Modeling hurricane waves and storm surge using integrally-coupled, scalable computations

J.C. Dietrich [a,*], M. Zijlema [b], J.J. Westerink [a], L.H. Holthuijsen [b], C. Dawson [c], R.A. Luettich Jr. [d], R.E. Jensen [e], J.M. Smith [e], G.S. Stelling [b], G.W. Stone [f]

[a] Department of Civil Engineering and Geological Sciences, University of Notre Dame, 156 Fitzpatrick Hall, Notre Dame, IN 46556, United States
[b] Faculty of Civil Engineering and Geosciences, Delft University of Technology, Stevinweg 1, 2628 CN, Delft, The Netherlands
[c] Institute for Computational Engineering and Sciences, University of Texas at Austin, 201 East 24 Street, Austin, TX 78712, United States
[d] Institute of Marine Sciences, University of North Carolina at Chapel Hill, 3431 Arendell Street, Morehead City, NC 28557, United States
[e] Coastal and Hydraulics Laboratory, U.S. Army Engineer Research and Development Center, 3909 Halls Ferry Road, Vicksburg, MS 39180, United States
[f] Coastal Studies Institute, Louisiana State University, Old Geology Building, Room 331, Baton Rouge, LA 70803, United States

ARTICLE INFO

ABSTRACT

The unstructured-mesh SWAN spectral wave model and the ADCIRC shallow-water circulation model have been integrated into a tightly-coupled SWAN + ADCIRC model. The model components are applied to an identical, unstructured mesh; share parallel computing infrastructure; and run sequentially in time. Wind speeds, water levels, currents and radiation stress gradients are vertex-based, and therefore can be passed through memory or cache to each model component. Parallel simulations based on domain decomposition utilize identical sub-meshes, and the communication is highly localized. Inter-model communication is intra-core, while intra-model communication is inter-core but is local and efficient because it is solely on adjacent sub-mesh edges. The resulting integrated SWAN + ADCIRC system is highly scalable and allows for localized increases in resolution without the complexity or cost of nested meshes or global interpolation between heterogeneous meshes. Hurricane waves and storm surge are validated for Hurricanes Katrina and Rita, demonstrating the importance of inclusion of the wave-circulation interactions, and efficient performance is demonstrated to 3062 computational cores.

© 2010 Elsevier B.V. All rights reserved.

1. Introduction

A broad energy spectrum exists in oceans, with wave periods ranging from seconds to months. Short waves, such as wind-driven waves and swell, have periods that range from 0.5 to 25 s. Longer waves, such as seiches, tsunamis, storm surges and tides, have periods that range from minutes to months. These short and long waves are well-separated in the energy spectrum and have well-defined spatial scales. This separation leads to distinct modeling approaches, depending on whether the associated scales can be resolved. For oceanic scales, short-wave models cannot resolve spatially or temporally the individual wind-driven waves or swell, and thus they treat the wave field as an energy spectrum and apply the conservation of wave action density to account for wave–current interactions. Long-wave models apply forms of conservation of mass and momentum, in two or three spatial dimensions, to resolve the circulation associated with processes such as tsunamis, storm surges or tides.

Although wind-driven waves and circulation are separated in the spectrum, they can interact. Water levels and currents affect the propagation of waves and the location of wave-breaking zones. Wave transformation generates radiation stress gradients that drive set-up and currents. Wind-driven waves affect the vertical momentum mixing and bottom friction, which in turn affect the circulation. Water levels can be increased by 5–20% in regions across a broad continental shelf, and by as much as 35% in regions of steep slope (Funakoshi et al., 2008; Dietrich et al., 2010). Thus, in many coastal applications, waves and circulation processes should be coupled.

Wave and circulation models have been limited by their spectral, spatial and temporal resolution. This limitation can be overcome by nesting structured meshes, to enhance resolution in specific regions by employing meshes with progressively finer scales. In a wave application, nesting also allows the use of models with different physics and numerics. Relatively fine nearshore wave models, such as STWAVE and SWAN, can be nested inside relatively coarse deep-water wave models, such as WAM and WaveWatch III (WAMDI Group, 1988; Komen et al., 1994; Booij et al., 1999; Smith et al., 2001;

* Corresponding author. Tel.: +1 574 631 3864.
 E-mail addresses: dietrich.15@nd.edu (J.C. Dietrich), m.zijlema@tudelft.nl (M. Zijlema), jjw@nd.edu (J.J. Westerink), l.h.holthuijsen@tudelft.nl (L.H. Holthuijsen), clint@ices.utexas.edu (C. Dawson), rick_luettich@unc.edu (R.A. Luettich), robert.e.jensen@usace.army.mil (R.E. Jensen), jane.m.smith@usace.army.mil (J.M. Smith), g.s.stelling@tudelft.nl (G.S. Stelling), gagreg@lsu.edu (G.W. Stone).
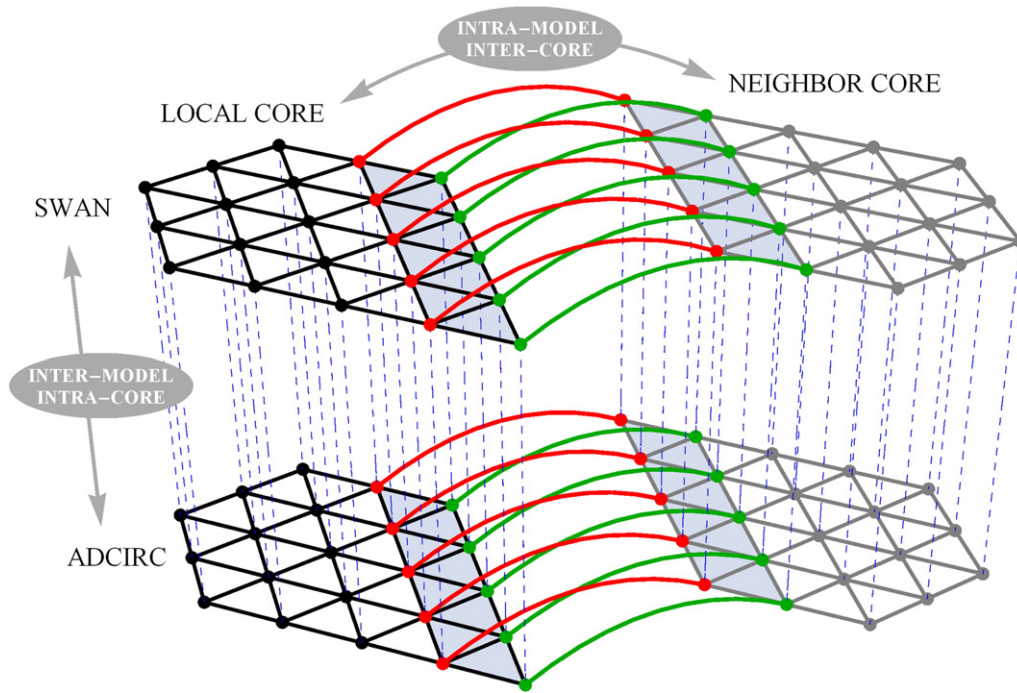
Fig. 1. Schematic of parallel communication between models and cores. Dashed lines indicate communication for all vertices within a sub-mesh, and are inter-model and intra-core. Solid lines indicate communication for the edge-layer-based nodes between sub-meshes, and are intra-model and inter-core.

Thompson et al., 2004; Gunther, 2005; Tolman, 2009). The nearshore wave models may not be efficient if applied to large domains, and the deep-water wave models may not contain the necessary physics or resolution for nearshore wave simulation. Until recently, wave models required nesting in order to vary resolution from basin to shelf to nearshore applications. These structured wave models can be coupled to structured circulation models that run on the same nested meshes (Kim et al., 2008).

Unstructured circulation models have emerged to provide localized resolution of gradients in geometry, bathymetry/topography, and flow processes. Resolution varies over a range of scales within the same mesh from deep water to the continental shelf to the channels, marshes and floodplains near shore (Westerink et al., 2008). Unstructured meshes allow for localized resolution where solution gradients are large and correspondingly coarser resolution where solution gradients are small, thus minimizing the computational cost relative to structured meshes with similar minimum mesh spacings.

The coupling of wave and circulation models has been implemented typically with heterogeneous meshes. A coupling application may have one unstructured circulation mesh and several structured wave meshes, and the models may pass information via external files (Funakoshi et al., 2008; Dietrich et al., 2010; Weaver and Slinn, 2004; Ebersole et al., 2007; Chen et al., 2008; Pandoe and Edge, 2008; Bunya et al., 2010). This 'loose' coupling is disadvantageous because it requires intra-model interpolation at the boundaries of the nested, structured wave meshes and inter-model interpolation between the wave and circulation meshes. This interpolation creates problems with respect to both accuracy and efficiency. Overlapping nested or adjacent wave meshes often have different solutions, and inter-mesh interpolation can smooth or enhance the integrated wave forcing. Furthermore, even if a component model is locally conservative, its interpolated solution will not necessarily be conservative. Finally, inter-model interpolation must be performed at all vertices of the meshes. This interpolation is problematic in a parallel computing environment, where the communication between sub-meshes is inter-model and semi-global. The sub-meshes must communicate on an area basis (i.e., the information at all vertices on a sub-mesh must

be shared). Global communication is costly and can prevent models from being scalable in high-performance computing environments.

An emerging practice is to couple models through a generic framework, such as the Earth System Modeling Framework (ESMF) (Hill et al., 2004; Collins et al., 2005), the Open Modeling Interface (OpenMI) Environment (Moore and Tindall, 2005; Gregersen et al., 2005) or the Modeling Coupling Toolkit (MCT) (Warner et al., 2008). These frameworks manage when and how the individual models are run, interpolate information between models if necessary, and make transparent the coupling to developers and users. However, these frameworks do not eliminate the fundamental problems of coupling when using heterogeneous meshes. Boundary conditions must be interpolated between nested, structured wave meshes, and water levels, currents and wave properties must be interpolated between
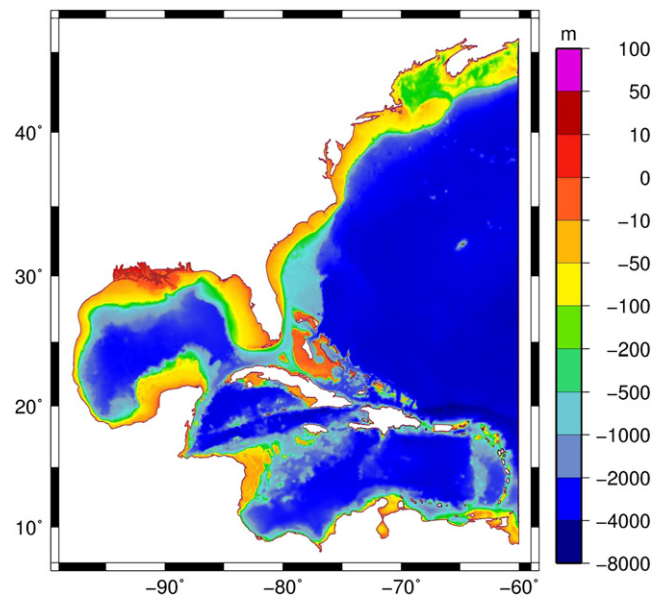

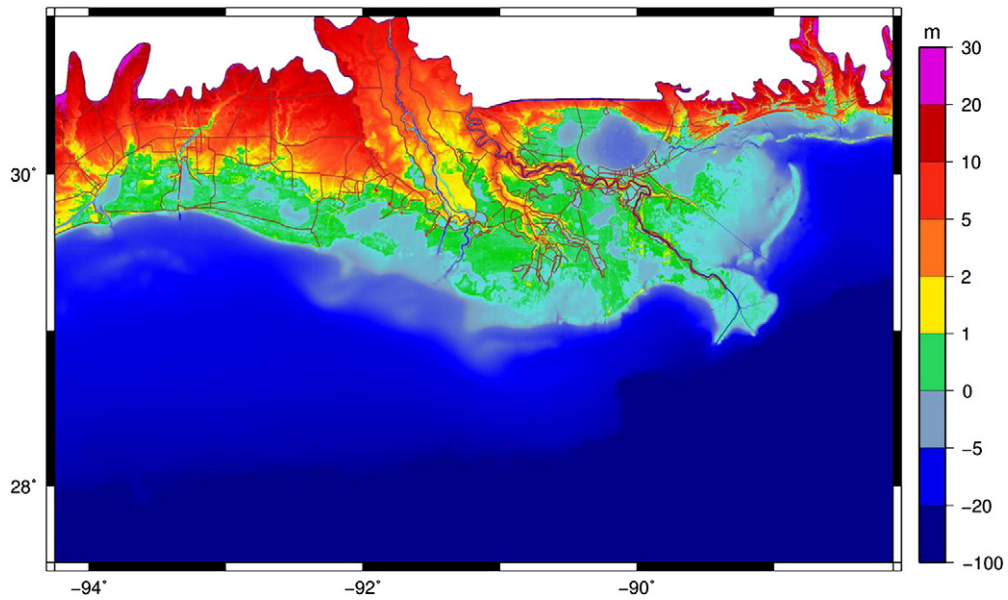**Fig. 2.** ADCIRC SL15 model domain with bathymetry (m).

Fig. 3. ADCIRC SL15 bathymetry and topography (m), relative to NAVD88 (2004.65), for southern Louisiana.

the unstructured circulation and structured wave meshes. This interpolation is costly, destroys the scalability of the coupled model, and thus limits the resolution that can be employed and the corresponding physics that can be simulated.

The recent introduction of unstructured wave models makes nesting unnecessary. Resolution can be enhanced nearshore and relaxed in deep water, allowing the model to simulate efficiently the wave evolution. SWAN has been used extensively to simulate waves in shallow water (Booij et al., 1999; Ris et al., 1999; Gorman and Neilson, 1999; Rogers et al., 2003), and it has been converted recently to run on unstructured meshes (Zijlema et al., 2010). This version of SWAN employs the unstructured-mesh analog to the solution technique from the structured version. It retains the physics and numerics of SWAN, but it runs on unstructured meshes, and it is both accurate and efficient in the nearshore and in deep water.

In this paper, we describe a 'tight' coupling of the SWAN wave model and the ADCIRC circulation model. SWAN and ADCIRC are run on the same unstructured mesh. This identical, homogeneous mesh allows the physics of wave-circulation interactions to be resolved correctly in both models. The unstructured mesh can be applied on a large domain to follow seamlessly all energy from deep to shallow water. There is no nesting or overlapping of structured wave meshes, and there is no inter-model interpolation. Variables and forces reside at identical, vertex-based locations. Information can be passed without interpolation, thus reducing significantly the communication costs.

In parallel computing applications, identical sub-meshes and communication infrastructure are used for both SWAN and ADCIRC, which run as the same program on the same computational core. All inter-model communication on a sub-mesh is done through local memory or cache. Communication between sub-meshes is intra-model. Information is passed only to the edges of neighboring sub-meshes, and thus the coupled model does not require global communication over areas. Domain decomposition places neighboring sub-meshes on neighboring cores, so communication costs are minimized. The coupled model is highly scalable and integrates
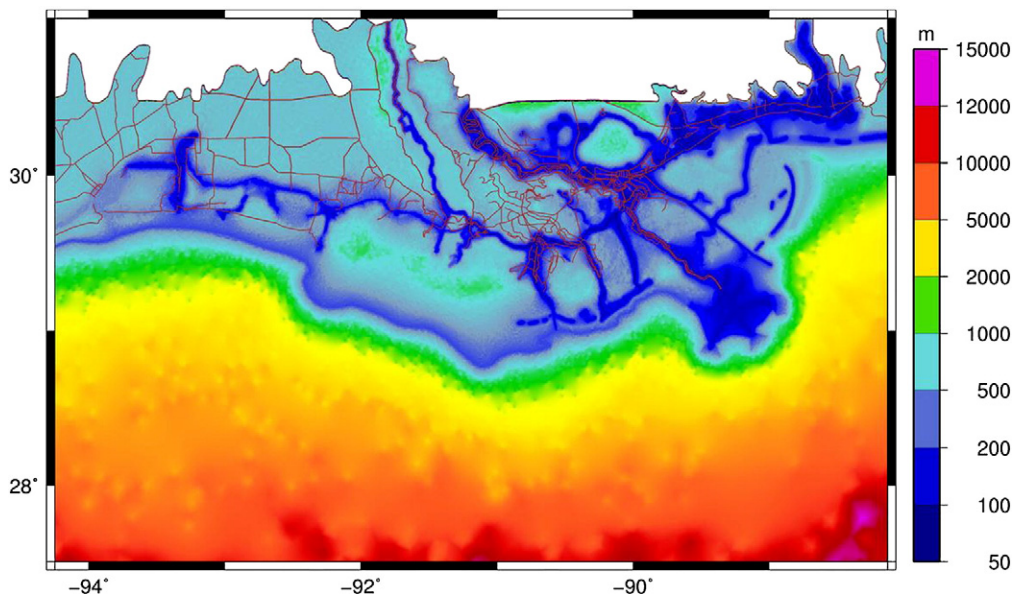

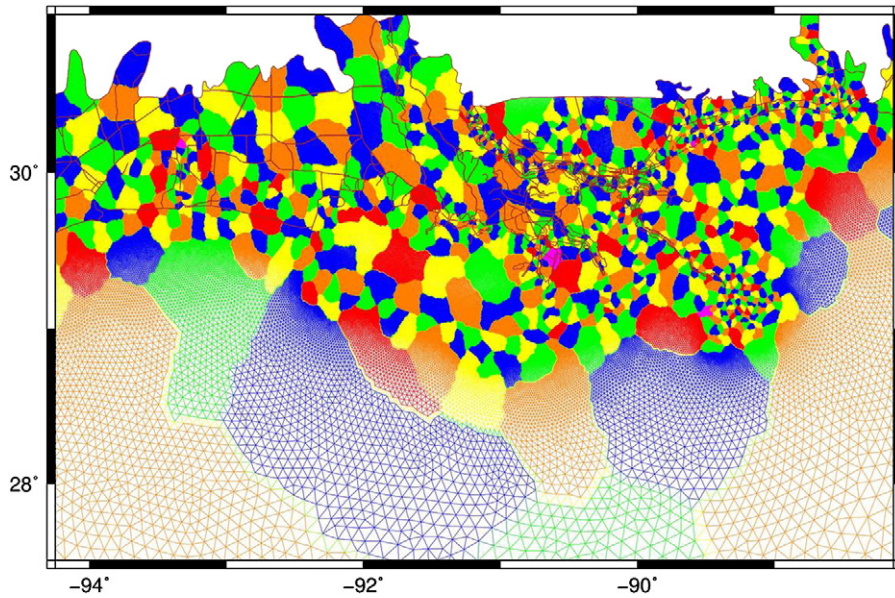**Fig. 4.** ADCIRC SL15 mesh resolution (m) in southern Louisiana.

Fig. 5. Example of the METIS domain decomposition of the ADCIRC SL15 mesh on 1014 computational cores. Colors indicate local sub-meshes and shared boundary layers.

seamlessly the physics and numerics from ocean to shelf to floodplain. Large domains and high levels of local resolution can be employed for both models, allowing the accurate depiction of the generation, propagation and dissipation of waves and surge. The resulting SWAN + ADCIRC model is suited ideally to simulate waves and circulation and their propagation from deep water to complicated nearshore systems.

In the sections that follow, the component SWAN and ADCIRC models are described, and the mechanics of their tight coupling is introduced. The coupled model is then validated through its application to hindcasts of Hurricanes Katrina and Rita. Finally, a benchmarking study shows SWAN + ADCIRC is highly scalable.

2. Methods

2.1. SWAN model

SWAN predicts the evolution in geographical space $\bar{x}$ and time t of the wave action density spectrum $N(\bar{x},t,\sigma,\theta)$, with σ the relative

frequency and θ the wave direction, as governed by the action balance equation (Booij et al., 1999):

$$\frac{\partial N}{\partial t} + \nabla_{\bar{x}} \cdot \left[\left(\bar{c}_g + \vec{U} \right) N \right] + \frac{\partial c_\theta N}{\partial \theta} + \frac{\partial c_\sigma N}{\partial \sigma} = \frac{S_{tot}}{\sigma}. \tag{1}$$

The terms on the left-hand side represent, respectively, the change of wave action in time, the propagation of wave action in $\bar{x}$-space (with $\nabla \bar{x}$ the gradient operator in geographic space, $\bar{c}_g$ the wave group velocity and $\vec{U}$ the ambient current vector), depth- and current-induced refraction and approximate diffraction (with propagation velocity or turning rate c_θ), and the shifting of σ due to variations in mean current and depth (with propagation velocity or shifting rate c_σ). The source term, S_{tot}, represents wave growth by wind; action lost due to whitecapping, surf breaking and bottom friction; and action exchanged between spectral components in deep and shallow water due to nonlinear effects. The associated SWAN parameterizations are given by Booij et al. (1999), with all subsequent modifications as

Table 1
Geographic location by type and number shown in Figs. 6 and 7.

|	
Rivers and channels	
1	Calcasieu Shipping Channel
2	Atchafalaya River
3	Mississippi River
4	Southwest Pass
Bays, lakes and sounds	
5	Sabine Lake
6	Calcasieu Lake
7	White Lake
8	Vermilion Bay
9	Terrebonne Bay
10	Timbalier Bay
11	Lake Pontchartrain
12	Lake Borgne
13	Gulf of Mexico
Islands	
14	Grand Isle
15	Chandeleur Islands
Places	
16	Galveston, TX
17	Tiger and Trinity Shoals
18	New Orleans, LA
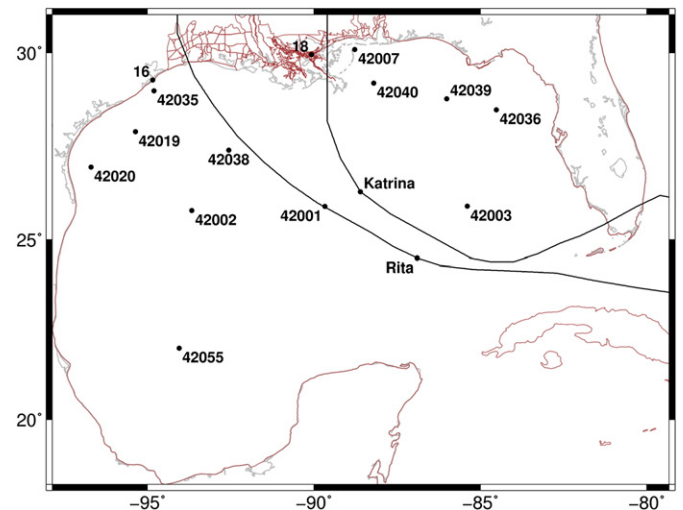
Fig. 6. Schematic of the Gulf of Mexico with locations of the 12 NDBC buoy stations used for the deep-water validation of SWAN during both Katrina and Rita. The hurricane tracks are also shown.

present in version 40.72, including the phase-decoupled refraction–diffraction (Holthuijsen et al., 2003), although diffraction is not enabled in the present simulations.

The unstructured-mesh version of SWAN implements an analog to the four-direction Gauss–Seidel iteration technique employed in the structured version, and it maintains SWAN's unconditional stability (Zijlema, 2010). SWAN computes the wave action density spectrum N ($\bar{x}, t, \sigma, \theta$) at the vertices of an unstructured triangular mesh, and it orders the mesh vertices so it can sweep through them and update the action density using information from neighboring vertices. It then sweeps through the mesh in opposite directions until the wave energy has propagated sufficiently through geographical space in all directions. It should be noted that, as a spectral model, SWAN does not attempt to represent physical processes at scales less than a wave length even in regions with very fine-scale mesh resolution. Phase-resolving wave models should be employed at these scales if sub-wave length scale flow features need to be resolved. However, this fine-scale mesh resolution may be necessary for other reasons, such as representing the complex bathymetry and topography of the region, or to improve the numerical properties of the computed solution.

2.2. ADCIRC model

ADCIRC is a continuous-Galerkin, finite-element, shallow-water model that solves for water levels and currents at a range of scales (Westerink et al., 2008; Luettich and Westerink, 2004; Atkinson et al., 2004; Dawson et al., 2006). Water levels are obtained through solution of the Generalized Wave Continuity Equation (GWCE):

$$\frac{\partial^2 \zeta}{\partial t^2} + \tau_0 \frac{\partial \zeta}{\partial t} + \frac{\partial \tilde{J}_x}{\partial x} + \frac{\partial \tilde{J}_y}{\partial y} - UH\frac{\partial \tau_0}{\partial x} - VH\frac{\partial \tau_0}{\partial y} = 0, \tag{2}$$

where:

$$\tilde{J}_x = -Q_x \frac{\partial U}{\partial x} - Q_y \frac{\partial U}{\partial y} + fQ_y - \frac{g}{2}\frac{\partial \zeta^2}{\partial x} - gH\frac{\partial}{\partial x}\left[\frac{P_s}{g\rho_0} - \alpha\eta\right]$$
$$+ \frac{\tau_{sx,wind} + \tau_{sx,waves} - \tau_{bx}}{\rho_0} + (M_x - D_x) + U\frac{\partial \zeta}{\partial t} + \tau_0 Q_x - gH\frac{\partial \zeta}{\partial x}, \tag{3}$$

$$\tilde{J}_y = -Q_x \frac{\partial V}{\partial x} - Q_y \frac{\partial V}{\partial y} - fQ_x - \frac{g}{2}\frac{\partial \zeta^2}{\partial y} - gH\frac{\partial}{\partial y}\left[\frac{P_s}{g\rho_0} - \alpha\eta\right]$$
$$+ \frac{\tau_{sy,wind} + \tau_{sy,waves} - \tau_{by}}{\rho_0} + \left(M_y - D_y\right) + V\frac{\partial \zeta}{\partial t} + \tau_0 Q_y - gH\frac{\partial \zeta}{\partial y}, \tag{4}$$

and the currents are obtained from the vertically-integrated momentum equations:

$$\frac{\partial U}{\partial t} + U\frac{\partial U}{\partial x} + V\frac{\partial U}{\partial y} - fV = -g\frac{\partial}{\partial x}\left[\zeta + \frac{P_s}{g\rho_0} - \alpha\eta\right]$$
$$+ \frac{\tau_{sx,winds} + \tau_{sx,waves} - \tau_{bx}}{\rho_0 H} + \frac{M_x - D_x}{H}, \tag{5}$$

and:

$$\frac{\partial V}{\partial t} + U\frac{\partial V}{\partial x} + V\frac{\partial V}{\partial y} + fU = -g\frac{\partial}{\partial y}\left[\zeta + \frac{P_s}{g\rho_0} - \alpha\eta\right]$$
$$+ \frac{\tau_{sy,winds} + \tau_{sy,waves} - \tau_{by}}{\rho_0 H} + \frac{M_y - D_y}{H}, \tag{6}$$

where $H = \zeta + h$ is the total water depth; ζ is the deviation of the water surface from the mean; h is the bathymetric depth; U and V are depth-integrated currents in the x- and y-directions, respectively; $Q_x = UH$ and $Q_y = VH$ are fluxes per unit width; f is the Coriolis parameter; g is the

gravitational acceleration; P_s is the atmospheric pressure at the surface; ρ_0 is the reference density of water; η is the Newtonian equilibrium tidal potential and α is the effective earth elasticity factor; $\tau_{s,winds}$ and $\tau_{s,waves}$ are surface stresses due to winds and waves, respectively; τ_b is the bottom stress; M are lateral stress gradients; D are momentum dispersion terms; and τ_0 is a numerical parameter that optimizes the phase propagation properties (Atkinson et al., 2004; Kolar et al., 1994). ADCIRC computes water levels ζ and currents U and V on an unstructured, triangular mesh by applying a linear Lagrange interpolation and solving for three degrees of freedom at every mesh vertex.

2.3. Sharing information

SWAN is driven by wind speeds, water levels and currents computed at the vertices by ADCIRC. Marine winds can be input to ADCIRC in a variety of formats, and these winds are adjusted directionally to account for surface roughness (Bunya et al., 2010). ADCIRC interpolates spatially and temporally to project these winds to the computational vertices, and then it passes them to SWAN. The water levels and ambient currents are computed in ADCIRC before being passed to SWAN, where they are used to recalculate the water depth and all related wave processes (wave propagation, depth-induced breaking, etc.).

The ADCIRC model is driven partly by radiation stress gradients that are computed using information from SWAN. These gradients $\tau_{s,waves}$ are computed by:

$$\tau_{sx,waves} = -\frac{\partial S_{xx}}{\partial x} - \frac{\partial S_{xy}}{\partial y}, \tag{7}$$

and:

$$\tau_{sy,waves} = -\frac{\partial S_{xy}}{\partial x} - \frac{\partial S_{yy}}{\partial y}, \tag{8}$$

where S_{xx}, S_{xy} and S_{yy} are the wave radiation stresses (Longuet–Higgins and Stewart, 1964; Battjes, 1972):

$$S_{xx} = \rho_0 g \iint \left(\left(n\cos^2\theta + n - \frac{1}{2}\right)\sigma N\right)d\sigma d\theta, \tag{9}$$

$$S_{xy} = \rho_0 g \iint (n\sin\theta\cos\theta\sigma N)d\sigma d\theta, \tag{10}$$

and:

$$S_{yy} = \rho_0 g \iint \left(\left(n\sin^2\theta + n - \frac{1}{2}\right)\sigma N\right)d\sigma d\theta, \tag{11}$$
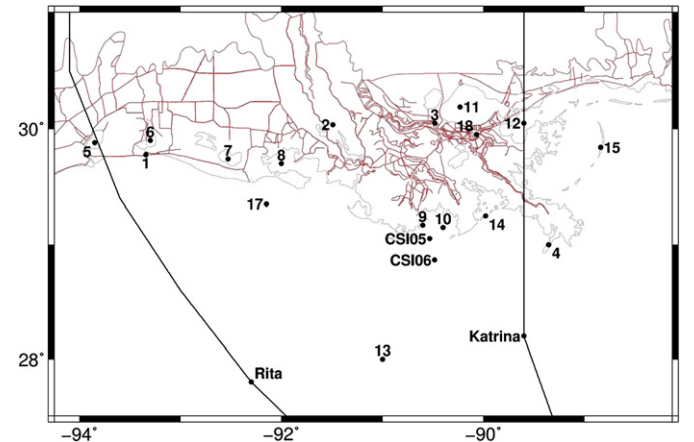

Fig. 7. Schematic of southern Louisiana with numbered markers of the locations listed in Table 1. Locations of the two CSI nearshore wave gauges and the hurricane tracks are also shown.

where *n* is the ratio of group velocity to phase velocity. The radiation stresses are computed at the mesh vertices using Eqs. (9)–(11). Then they are interpolated into the space of continuous, piecewise linear functions and differentiated to obtain the gradients in Eqs. (7) and (8), which are constant on each element. These element-based gradients are projected to the vertices by taking an area-weighted average of the gradients on the elements adjacent to each vertex.

2.4. Coupling procedure

ADCIRC and SWAN run in series on the same local mesh and core. The two models "leap frog" through time, each being forced with information from the other model.

Because of the sweeping method used by SWAN to update the wave information at the computational vertices, it can take much
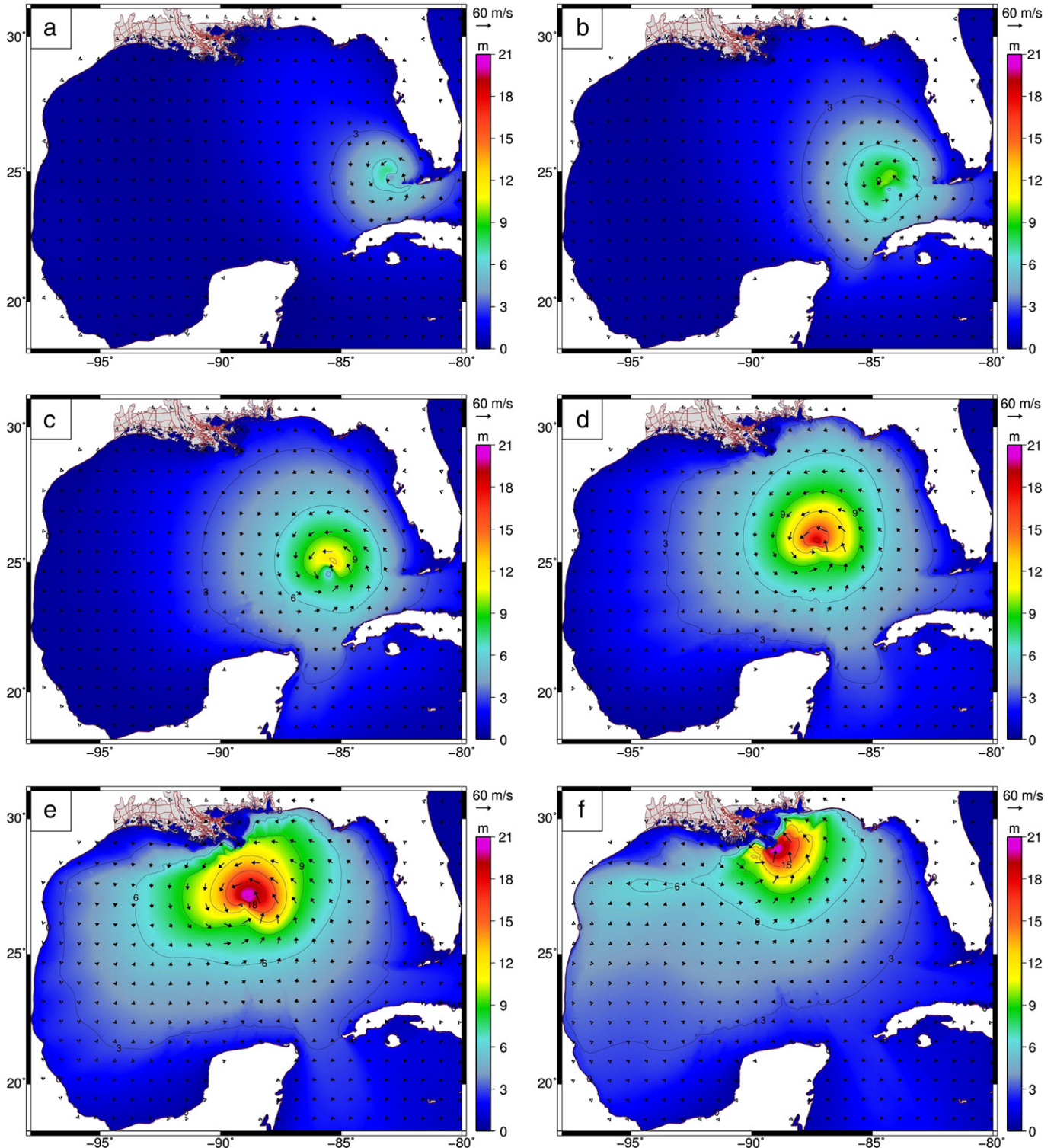

Fig. 8. Hurricane Katrina significant wave height contours (m) and wind speed vectors (m s^{-1}) at 12-h intervals in the Gulf of Mexico. The six panels correspond to the following times: (a) 2200 UTC 26 August 2005, (b) 1000 UTC 27 August 2005, (c) 2200 UTC 27 August 2005, (d) 1000 UTC 28 August 2005, (e) 2200 UTC 28 August 2005 and (f) 1000 UTC 29 August 2005.

larger time steps than ADCIRC, which is diffusion- and also Courant-time-step limited due to its semi-explicit formulation and its wetting-and-drying algorithm. For that reason, the coupling interval is taken to be the same as the SWAN time step. On each coupling interval, ADCIRC is run first, because we assume that, in the nearshore and the coastal floodplain, wave properties are more dependent on circulation.

At the beginning of a coupling interval, ADCIRC can access the radiation stress gradients computed by SWAN at times corresponding to the beginning and end of the previous interval. ADCIRC uses that information to extrapolate the gradients at all of its time steps in the current interval. These extrapolated gradients are used to force the ADCIRC solution as described previously. Once the ADCIRC stage is finished, SWAN is run for one time step, to bring it to the same moment in time as ADCIRC. SWAN can access the wind speeds, water levels and currents computed at the mesh vertices by ADCIRC, at times corresponding to the beginning and end of the current interval. SWAN applies the mean of those values to force its solution on its time step. In this way, the radiation stress gradients used by ADCIRC are always extrapolated forward in time, while the wind speeds, water levels and currents used by SWAN are always averaged over each of its time steps.

2.5. Parallel coupling framework

The METIS domain-decomposition algorithm is applied to distribute the global mesh over a number of computational cores (Karypis and Kumar, 1999). The decomposition minimizes inter-core communication by creating local sub-meshes with small ratios of the number of vertices within the domain to the number of shared vertices at sub-mesh interfaces. The decomposition also balances the computational load by creating local sub-meshes with a similar number of vertices; the local meshes decrease in geographical area as their average mesh size is decreased.

A schematic of the communication is shown in Fig. 1. Each local core has a sub-mesh that shares a layer of boundary elements with the sub-meshes on its neighbor cores. To update the information at these boundaries in either model, information is passed at the shared vertices on each sub-mesh. This communication is local between adjacent sub-meshes. Furthermore, only a small fraction of the vertices on any sub-mesh are shared. Thus the parallel, inter-core communication is localized and efficient.

SWAN and ADCIRC utilize the same local sub-meshes. Information is stored at the vertices in both models, so it can be passed through local memory or cache, without the need for any network-based, inter-core communication. In contrast to loose coupling paradigms, in which the model components run on different sub-meshes and different cores, SWAN + ADCIRC does not destroy its scalability by interpolating semi-globally. The inter-model communication is intra-core.

3. Hindcasts of Katrina and Rita

3.1. Parameters of hindcasts

SWAN + ADCIRC will utilize the SL15 mesh that has been validated for applications in southern Louisiana (Dietrich et al., 2010; Bunya
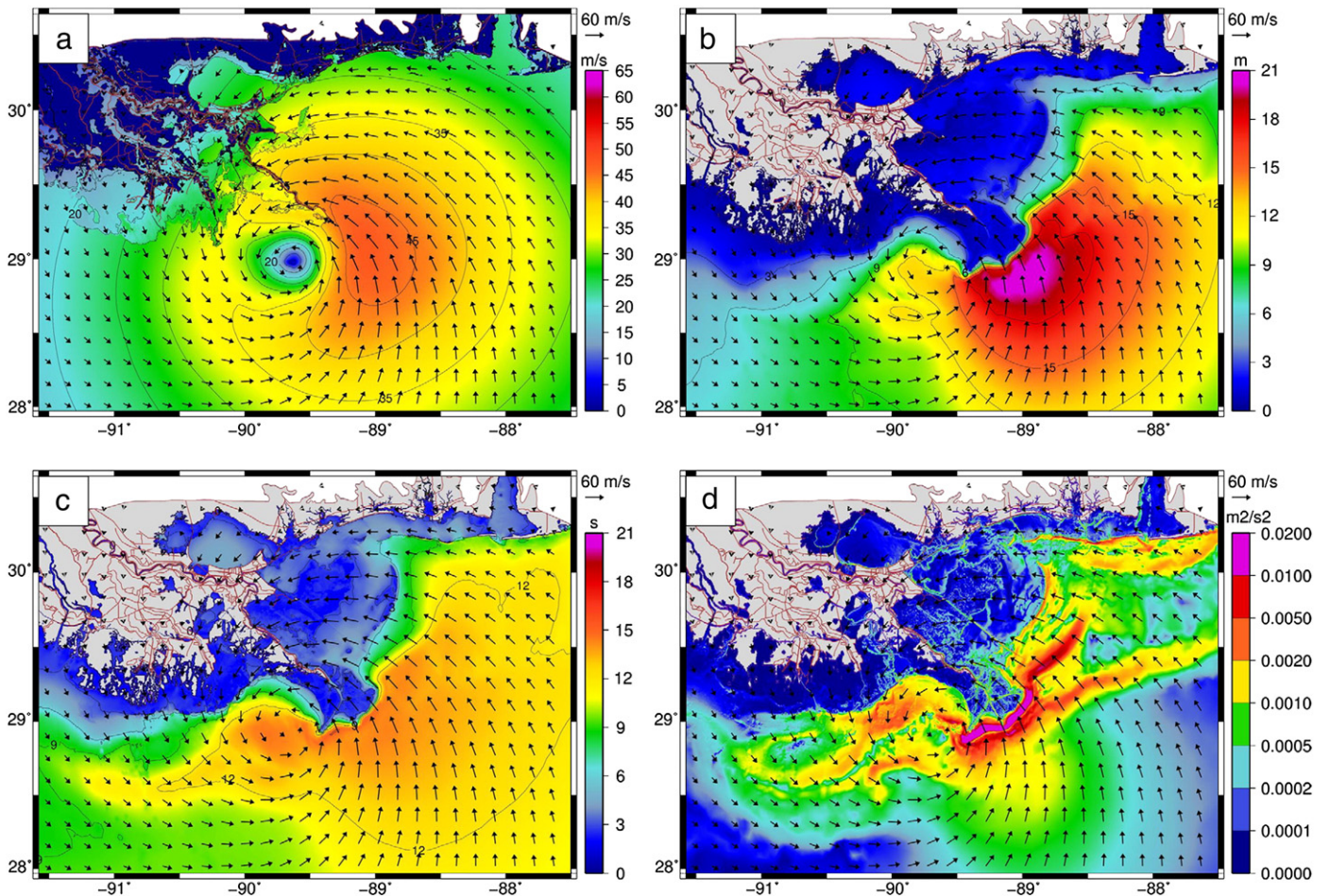

Fig. 9. Hurricane Katrina winds and waves at 1000 UTC 29 August 2005 in southeastern Louisiana. The panels are: (a) wind contours and vectors (m s^{-1}), shown with a 10 min averaging period and at 10 m elevation; (b) significant wave height contours (m) and wind vectors (m s^{-1}); (c) mean wave period contours (s) and wind vectors (m s^{-1}); and (d) radiation stress gradient contours (m2 s^{-2}) and wind vectors (m s^{-1}).

et al., 2010). The complex bathymetry/topography and mesh resolution are shown in Figs. 2–4. This mesh incorporates local resolution down to 50 m, but also extends to the Gulf of Mexico and the western North Atlantic Ocean. It includes a continental shelf that narrows near the protruding delta of the Mississippi River, sufficient resolution of the wave-transformation zones near the delta and over the barrier islands, and intricate representation of the various natural and man-made geographic features that collect and focus storm surge in this region. The SL15 mesh contains 2,409,635 vertices and 4,721,496 triangular elements. An example of the METIS domain decomposition of the SL15 mesh on 1014 cores is shown in Fig. 5. Local sub-meshes are shown in separate colors, and the cores communicate via the layers of overlapping elements that connect these local meshes. Each parallel core utilizes the same unstructured local sub-mesh for both SWAN and ADCIRC. Notable geographic locations are summarized in Table 1 and shown in Figs. 6 and 7.

SWAN + ADCIRC has been validated via hindcasts of Katrina and Rita, which utilize optimized wind fields developed with an Interactive Objective Kinematic Analysis (IOKA) System (Cox et al., 1995; Cardone et al., 2007). The Katrina wind fields also have an inner core that is data-assimilated from NOAA's Hurricane Research Division Wind Analysis System (H*WIND) (Powell et al., 1996, 1998). The wind speeds are referenced to 10 m in height, peak 30 min averaged "sustained" wind speed, and marine exposure. They contain snapshots at 15 min intervals on a regular 0.05° grid. The

wind fields are read by ADCIRC, and then each local core interpolates onto its local sub-mesh.

With the lone exception of the source of its radiation stress gradients, ADCIRC uses the same parameters as discussed in Bunya et al. (2010). The water levels are adjusted for the regional difference between LMSL and NAVD88 (2004.65) and the seasonal fluctuation in sea level in the Gulf of Mexico. Bottom friction is parameterized using a Manning's n formulation, with spatially-variable values based on land classification. The Mississippi and Atchafalaya Rivers are forced with flow rates that are representative of the conditions during the storms. In addition, seven tidal constituents are forced on the open boundary in the Atlantic Ocean. ADCIRC applies a wind drag coefficient due to Garratt (1977) with a cap of $C_d \leq 0.0035$.

The SWAN time step and the coupling interval are 600 s. The SWAN frequencies range from 0.031 to 0.548 Hz and are discretized into 30 bins on a logarithmic scale ($\Delta\sigma/\sigma \approx 0.1$). The wave directions are discretized into 36 sectors, each sector representing 10°. The present simulations use the SWAN default for wind input based on Snyder et al. (1981) and the modified whitecapping expression of Rogers et al. (2003), which yields less dissipation in lower frequency components and better prediction of the wave periods compared to the default formulation of Hasselmann (1974). Quadruplet nonlinear interactions are computed with the Discrete Interaction Approximation (Hasselmann et al., 1985). For the shallow-water source terms, depth-induced breaking is computed with a spectral version of the
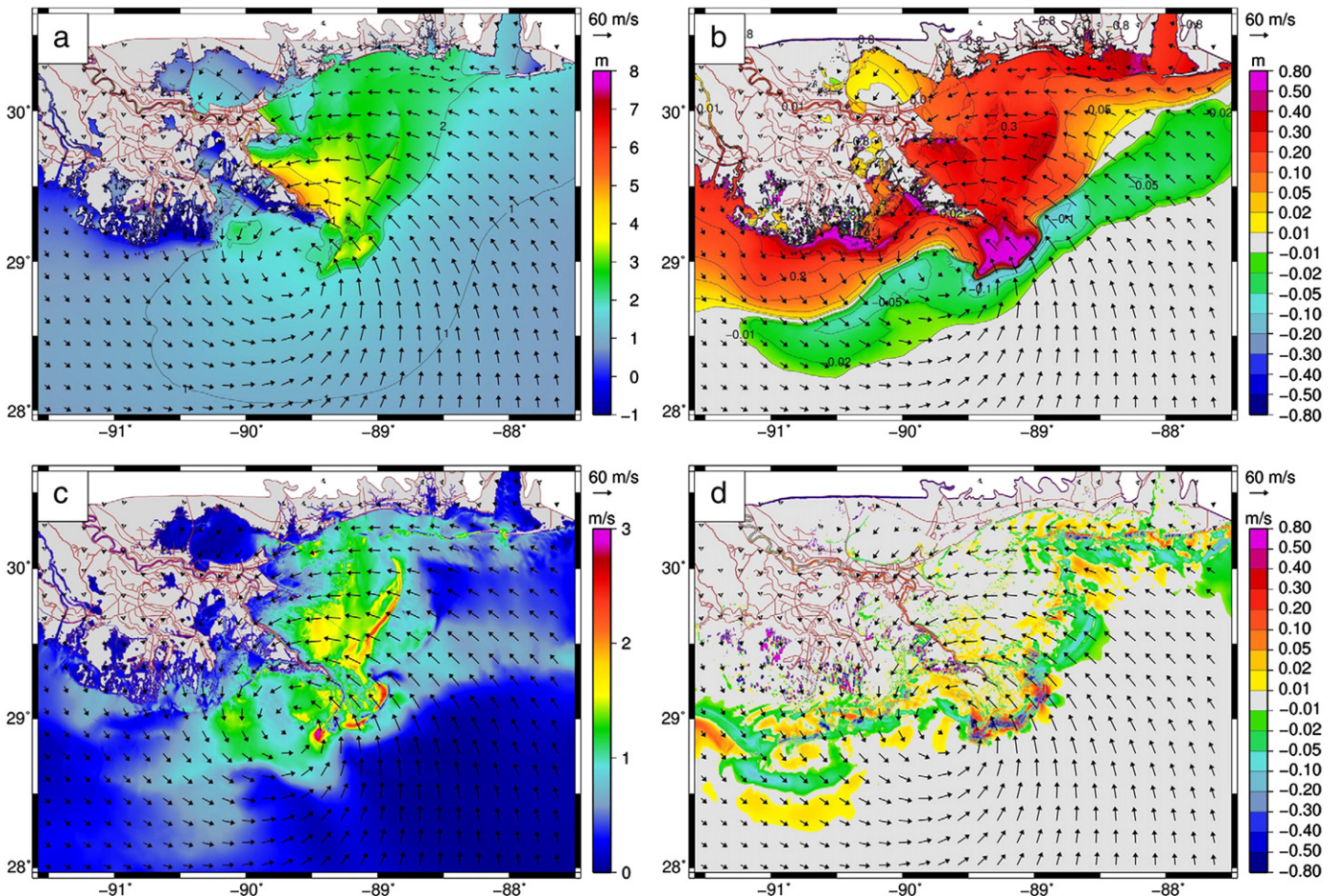

Fig. 10. Hurricane Katrina water levels and currents at 1000 UTC 29 August 2005 in southeastern Louisiana. The panels are: (a) water level contours (m) and wind vectors (m s^{-1}); (b) wave-driven set-up contours (m) and wind vectors (m s^{-1}); (c) current contours (m s^{-1}) and wind vectors (m s^{-1}); and (d) wave-driven current contours (m s−1) and wind vectors (m s^{-1}).

model due to Battjes and Janssen (1978) with the breaking index $\gamma = 0.73$, bottom friction is based on the JONSWAP formulation (Hasselmann et al., 1973) with friction coefficient $C_b = 0.067 \text{ m}^2 \text{ s}^{-3}$, and the triad nonlinear interactions are computed with the Lumped Triad Approximation of Eldeberky (1996). Although the resolution in the SL15 mesh is well-suited to simulate waves and surge along the coastlines of Louisiana, Mississippi and Alabama, its relatively coarse resolution in the Caribbean Sea and Atlantic Ocean can create spurious wave refraction over one spatial element. Thus, wave refraction is enabled only in the computational sub-meshes in which the resolution of the bathymetry is sufficient, specifically in the northern Gulf of Mexico. SWAN applies a wind drag coefficient due to Wu (1982) with a cap of $C_d \leq 0.0035$.

In the validation sections that follow, the SWAN wave quantities will be compared to the measured data and also to the solution from a loose coupling to structured versions of WAM and STWAVE. WAM was run on a regular 0.05° mesh with coverage of the entire Gulf of Mexico, while STWAVE was run on four or five nested sub-meshes with resolution of 200 m and coverage of southern Louisiana, Mississippi and Alabama. The details of this loose coupling can be found in Bunya et al. (2010) and Dietrich et al. (2010). For the validation herein, wave parameters from WAM and STWAVE were integrated to 0.41 Hz, while parameters from SWAN were integrated to 0.55 Hz.

3.2. Hurricane Katrina

Katrina is a good validation case because of its size and scope. It was a large hurricane, with waves of 16.5 m measured off the continental shelf and storm surge of 8.8 m measured along the Mississippi coastline. But it also generated waves and storm surge over multiple scales and impacted the complex topography and levee protection system of southeastern Louisiana. To simulate the evolution of this hurricane, the coupled model must describe the system in rich detail and integrate seamlessly all of its components.

3.2.1. Evolution of waves in deep water

Because SWAN has not been used traditionally in deep water, we examine the behavior of its solution as Katrina moved through the Gulf of Mexico. Fig. 8 depicts the computed significant wave heights at 12 h intervals as Katrina enters the Gulf, generates waves throughout the majority of the basin, and then makes landfall in southern Louisiana. In its early stages, Katrina generated significant wave heights of 6–9 m in the eastern half of the Gulf. However, as the storm strengthened on 28 August 2005, the significant wave heights increased to a peak of about 22 m at 2200 UTC, and waves of at least 3 m were generated throughout most of the Gulf. The impact of the hurricane on waves was widespread and dramatic.
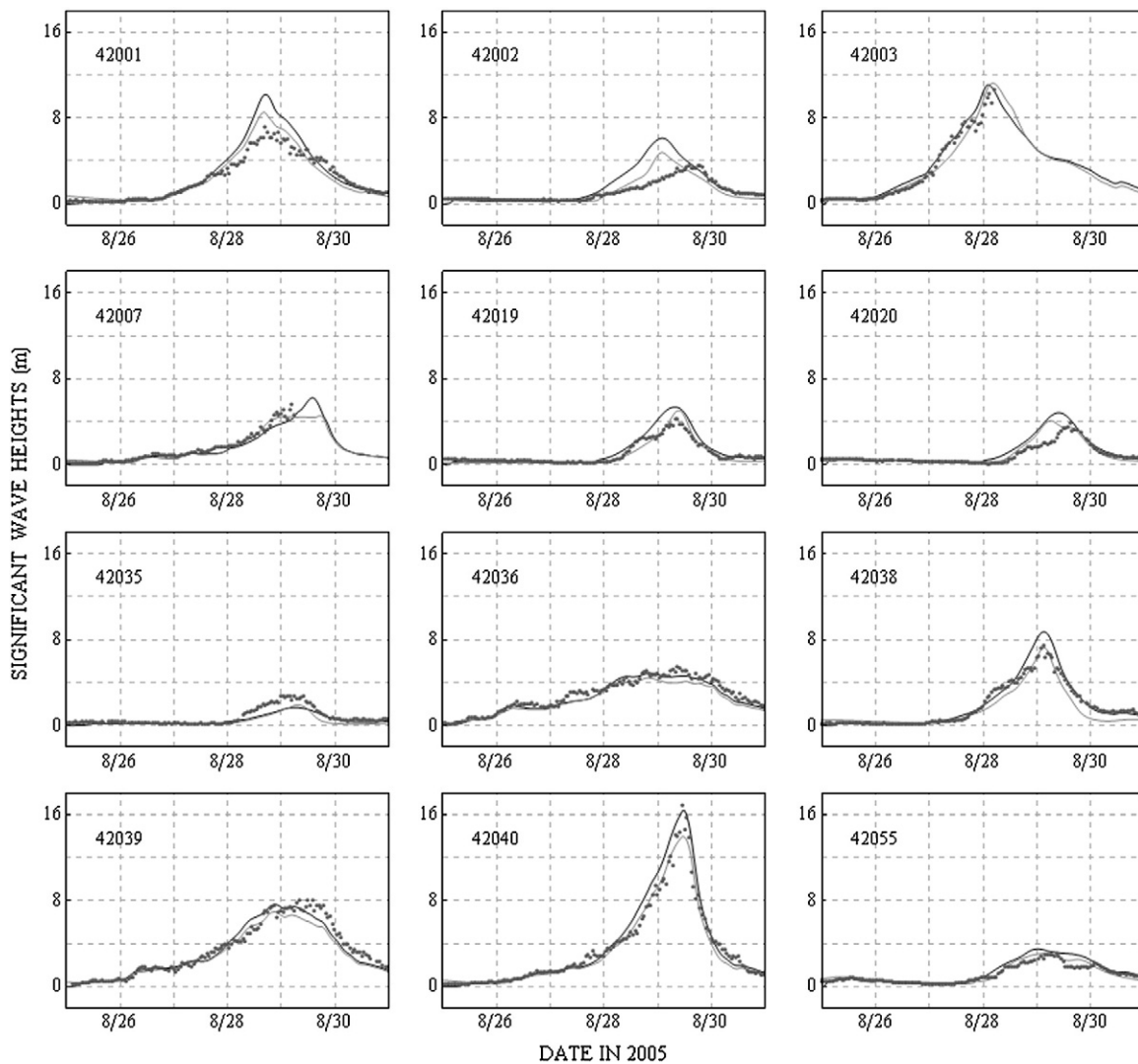
Fig. 11. Significant wave heights (m) during Hurricane Katrina at 12 NDBC buoys. The measured data is shown with black dots, the modeled SWAN results are shown with black lines, and the modeled WAM results are shown with gray lines.

The unstructured mesh used by SWAN + ADCIRC captures this evolution. Relatively coarse mesh resolution of 12–18 km is applied in the Gulf to capture the generation of waves in deep water and their propagation onto the continental shelf, and relatively fine (but locally still fairly coarse) resolution of 200–500 m is applied in the wave-breaking zones. It is unnecessary to change meshes or interpolate boundary conditions or solutions as would be required for nesting structured meshes.

3.2.2. Interaction of processes at landfall

We examine the system at 1000 UTC 29 August 2005, shortly before Katrina's landfall along the southern reach of the Mississippi River. Katrina is pushing its largest waves onto the continental shelf. Fig. 9a shows the wind field in southeastern Louisiana. The eye is located less than 50 km and 90 min from landfall, and it is just west of Southwest Pass. The highest wind speeds of 45–50 m s^{-1} are located over the bird's foot of the Mississippi River delta, but winds of 25–40 m s^{-1} are blowing easterly and southeasterly over much of the continental shelf.

As shown in Fig. 9b, the largest computed waves are generated in the Gulf and experience depth-limited breaking as they move onto the continental shelf. In regions where the shelf is narrow, the waves transform over short distances. To the south of the Mississippi River delta, waves of 18–19 m are breaking where the bathymetry changes

rapidly. To the east, near the Chandeleur Islands, the continental shelf is broader, and the wave heights decrease gradually as they move onto the shelf and over the barrier islands. Behind these initial breaking zones, smaller waves are generated and dissipated. In Lake Pontchartrain, northerly winds generate waves of 1.5–2 m that break along the northern edge of New Orleans. This behavior is mirrored in the mean periods shown in Fig. 9c, in which there is a clear difference between the long-period waves generated in deep water and the short-period waves generated behind the initial breaking zones.

As these waves break, they exert a stress on the water column that changes water levels and/or drives currents. As shown in Fig. 9d, the largest radiation stress gradients of 0.02 m^2 s^{-2} are located at the south edge of the delta, where the largest waves are breaking. However, radiation stress gradients also exist on the continental shelf, over barrier islands, inside the marshes, and along coastlines. Because both models are running on the same local sub-mesh, the complexities of the SWAN solution are passed directly to ADCIRC.

The ADCIRC water levels are shown in Fig. 10a. Easterly winds are pushing storm surge of 2–3 m onto the continental shelf, and 5 m of surge has built against the river levees. This surge will release northward as Katrina moves through the system and eventually makes landfall along the Mississippi coastline. However, significant flooding is occurring already in the marshes of southeast Louisiana. Some of this flooding is due to the wave set-up shown in Fig. 10b. The
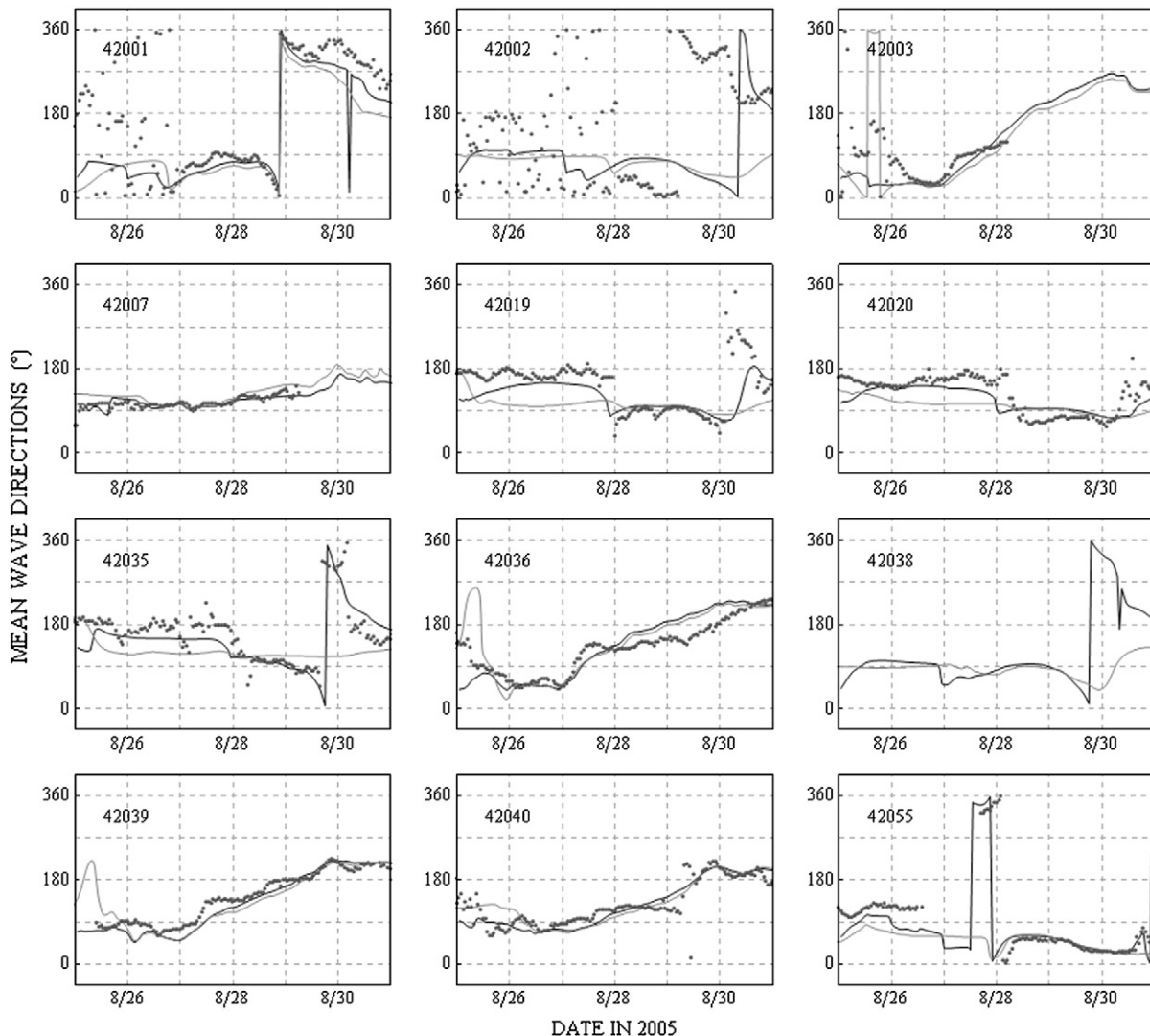

Fig. 12. Mean wave directions (°), measured clockwise from geographic north, during Hurricane Katrina at 12 NDBC buoys. The measured data is shown with black dots, the modeled SWAN results are shown with black lines, and the modeled WAM results are shown with gray lines.

Fig. 13. Mean wave periods (s) during Hurricane Katrina at 12 NDBC buoys. The measured data is shown with black dots, the modeled SWAN results are shown with black lines, and the modeled WAM results are shown with gray lines.
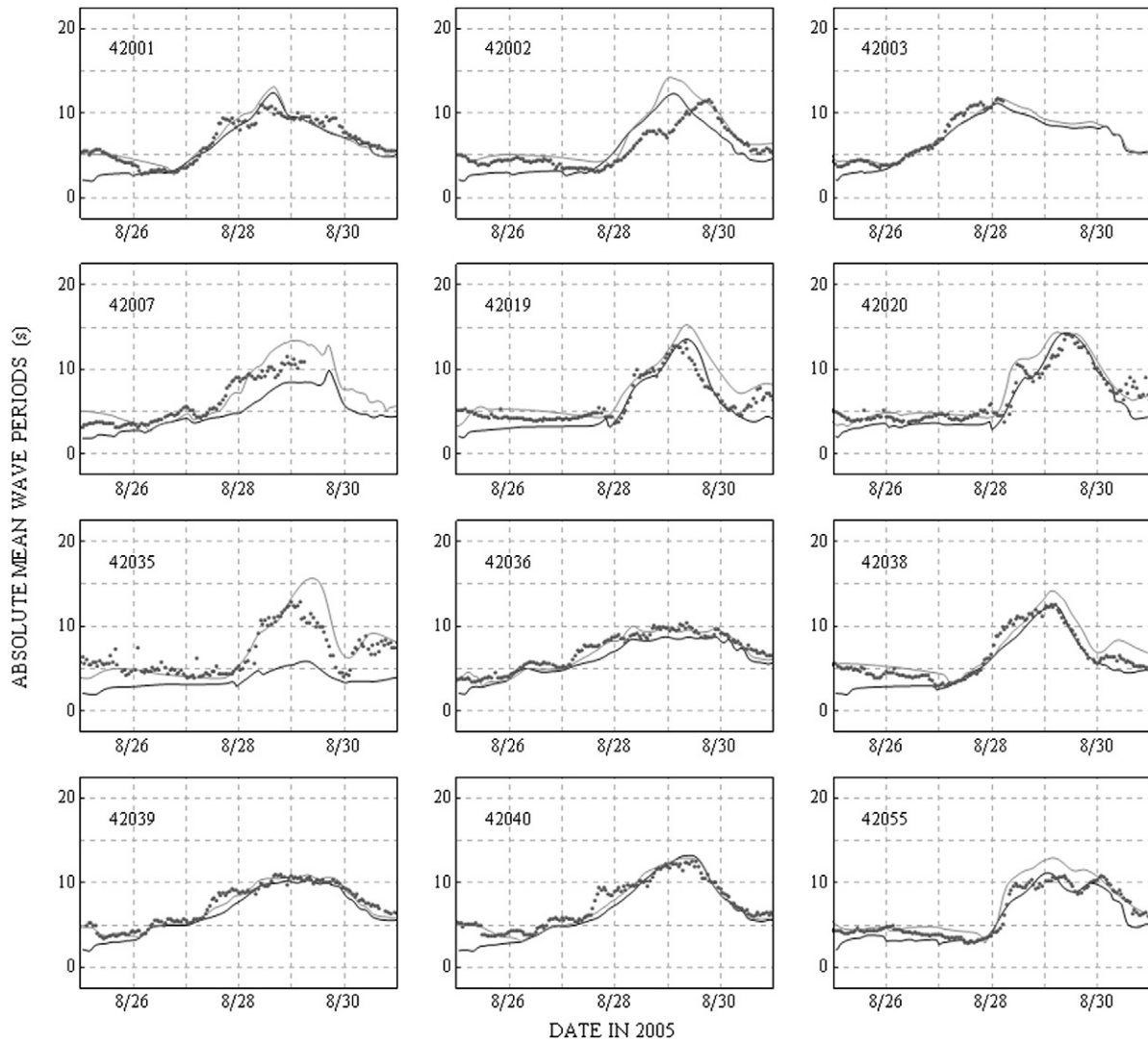
stresses associated with wave breaking increased the overall water levels by 0.2–0.3 m over much of the region, and by as much as 0.8 m in the delta. These contributions range from 5 to 35% of the overall water level.

As shown in Fig. 10c, the currents are significant throughout the region, with a range of 0.5–1.5 m s^{-1} on the continental shelf. As surge is pushed through Lake Borgne and into Lake Pontchartrain, the currents in the passes increase to 1.5–2.5 m s^{-1}. Similar currents are observed over the barrier islands and the delta, where waves are breaking. As shown in Fig. 10d, the wave stresses increase the currents in these regions. In the bird's foot of the delta, the wave-driven currents are 0.1–0.3 m s^{-1}, or about 5–10% of the overall currents in this region. The tightly-coupled SWAN + ADCIRC model does not have anomalies near boundaries, does not exhibit inconsistent solutions anywhere within the domain (as is possible with overlapping structured-mesh models), and the simulation increases dramatically in efficiency.

3.2.3. Validation of coupled model

SWAN + ADCIRC has been validated to several sets of measurement data. In deep water, the National Data Buoy Center (NDBC) collected and analyzed wave measurements at 12 buoys shown in Fig. 6. Figs. 11–13

compare measured significant heights, mean directions and mean periods to computed values from SWAN + ADCIRC as well as WAM. SWAN matches the magnitude and timing of the peaks at most buoys. For example, the modeled significant wave height of 16 m at buoy 42040 is very close to the measured peak height of 16.5 m. Similar behavior is seen with respect to directions and periods. At some buoys, errors are caused by a combination of missing physics and/or measurement error. At a few buoys to the west of the track, such as 42001, 42002, 42019 and 42020, the match is not as good as at other locations, possible reasons include the presence of a warm-core eddy (Wang and Oey, 2008), which is not included in the circulation model.

Table 2

Summary of analysis timeframes for the three wave models. The errors shown in Table 3–4 were computed over the timeframes listed herein.

Storm	Model	Beginning of analysis	End of analysis
Katrina	SWAN	2005/08/25/0100Z	2005/08/31/2300Z
	WAM	2005/08/24/0100Z	2005/08/31/0600Z
	WAM/STWAVE	2005/08/28/1215Z	2005/08/30/1145Z
Rita	SWAN	2005/09/18/0100Z	2005/09/24/2300Z
	WAM	2005/09/18/0015Z	2005/09/25/0000Z
	WAM/STWAVE	2005/09/22/1830Z	2005/09/24/1800Z

Furthermore mesh resolution, especially the 12–18 km mesh sizes in the central Gulf, is also relatively coarse in these regions. When the waves were small in the days leading up to the storm (8/25–27), the measured mean directions tend to be noisy, which increases the model-to-measurement differences. A quantitative comparison was performed by computing the scatter index (SI):

$$SI = \frac{\sqrt{\frac{1}{N}\sum_{i=1}^{N}(S_i - O_i)^2}}{\frac{1}{N}\sum_{i=1}^{N}O_i}, \tag{12}$$

the relative bias parameter:

$$Relative\,Bias = \frac{\frac{1}{N}\sum_{i=1}^{N}(S_i - O_i)}{\frac{1}{N}\sum_{i=1}^{N}O_i}, \tag{13}$$

and the mean observation:

$$Mean\,Obs. = \frac{1}{N}\sum_{i=1}^{N}O_i, \tag{14}$$

where N is the total number of data, O_i is the measured value and S_i is the modeled value. These metrics are summarized in Table 3, although the metrics for the mean directions are not normalized because the reference direction is arbitrary. The differences in the mean observations for each model reflect the differences in the time periods over which the errors were computed, as shown in Table 2. The relative

bias in SWAN is caused mostly by a time shift between its results and the measured data; SWAN does not match exactly the timing of the peak. The SI errors are large compared to other wave studies (Cardone et al., 1996; Janssen, 2004), but they reflect the complexities of modeling hurricane systems that change rapidly over multiple scales. In deep water, the errors in the SWAN results are only slightly larger than in the WAM results, even though the SWAN mesh spacing of 12–18 km is much larger than WAM's regular mesh spacing of 5 km.

It is more difficult to validate SWAN in shallow water because of the scarcity of nearshore measurement data. The Coastal Studies Institute at Louisiana State University operates two gauges south of Terrebonne Bay, as shown in Fig. 7 (http://www.wavcis.lsu.edu). Stations CSI05 and CSI06 are located in water depths of about 7 m and 20 m, respectively, so they experience the nearshore physics of bottom friction, triad wave–wave interactions and depth-induced breaking. As shown in Fig. 14, SWAN matches well the wave parameters at these stations. As shown in Table 4, the average errors produced by WAM/STWAVE are somewhat smaller than those produced by SWAN, presumably because of the better estimate of the deep-water wave conditions.

The ADCIRC water levels have been validated to high-water marks (HWMs) collected at 206 stations by the USACE and 193 stations by URS/FEMA (Ebersole et al., 2007; URS, 2006a). These HWMs include the effects of surge and wave set-up but not wind waves. ADCIRC predicts well the majority of the HWMs, with most locations having differences less than 0.5 m. Comparisons of measured-to-modeled HWMs have best-fit slopes of 0.98–1.02 and correlation coefficients R^2 of 0.92–0.94. Differences occur in places where the resolution is insufficient, such as on the south shore of Lake Pontchartrain, but the match to the HWMs is much better in regions near open water. Average magnitudes and standard deviations of the differences were
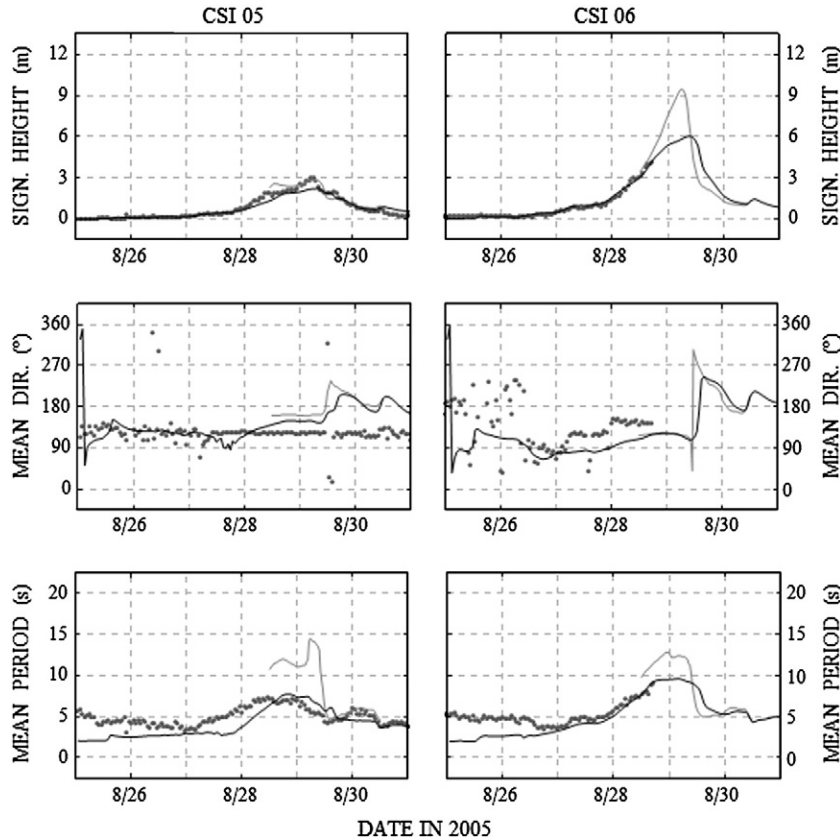

Fig. 14. Hurricane Katrina significant wave heights (m); mean wave directions (°), measured clockwise from geographic north; and mean wave periods (s) at two CSI buoys. The measured data is shown with black dots, the modeled SWAN results are shown with black lines, and the modeled WAM/STWAVE results are shown with gray lines. The CSI buoy data was collected by WAVCIS (http://www.wavcis.lsu.edu).

computed, both with and without the errors in the measurement data, and those values are summarized in Table 5. When we account for the HWM uncertainties, the estimated average absolute model error is 0.26–0.27 m, and the standard deviation is 0.41–0.44 m.

These error statistics are similar to results obtained from the loose coupling of ADCIRC to the structured wave models WAM and STWAVE (Bunya et al., 2010). In addition, a qualitative comparison

to that study shows the SWAN + ADCIRC solution is remarkably similar. Because the wave set-up in Fig. 10b is shown near the peak of the hurricane, it can be compared to the maximum wave set-up obtained from the loose coupling (Dietrich et al., 2010). Both coupled models create set-up of 0.8 m over the Mississippi River delta and 0.2–0.3 m over much of the region. WAM/STWAVE is slightly more focused, with higher wave set-up behind the barrier
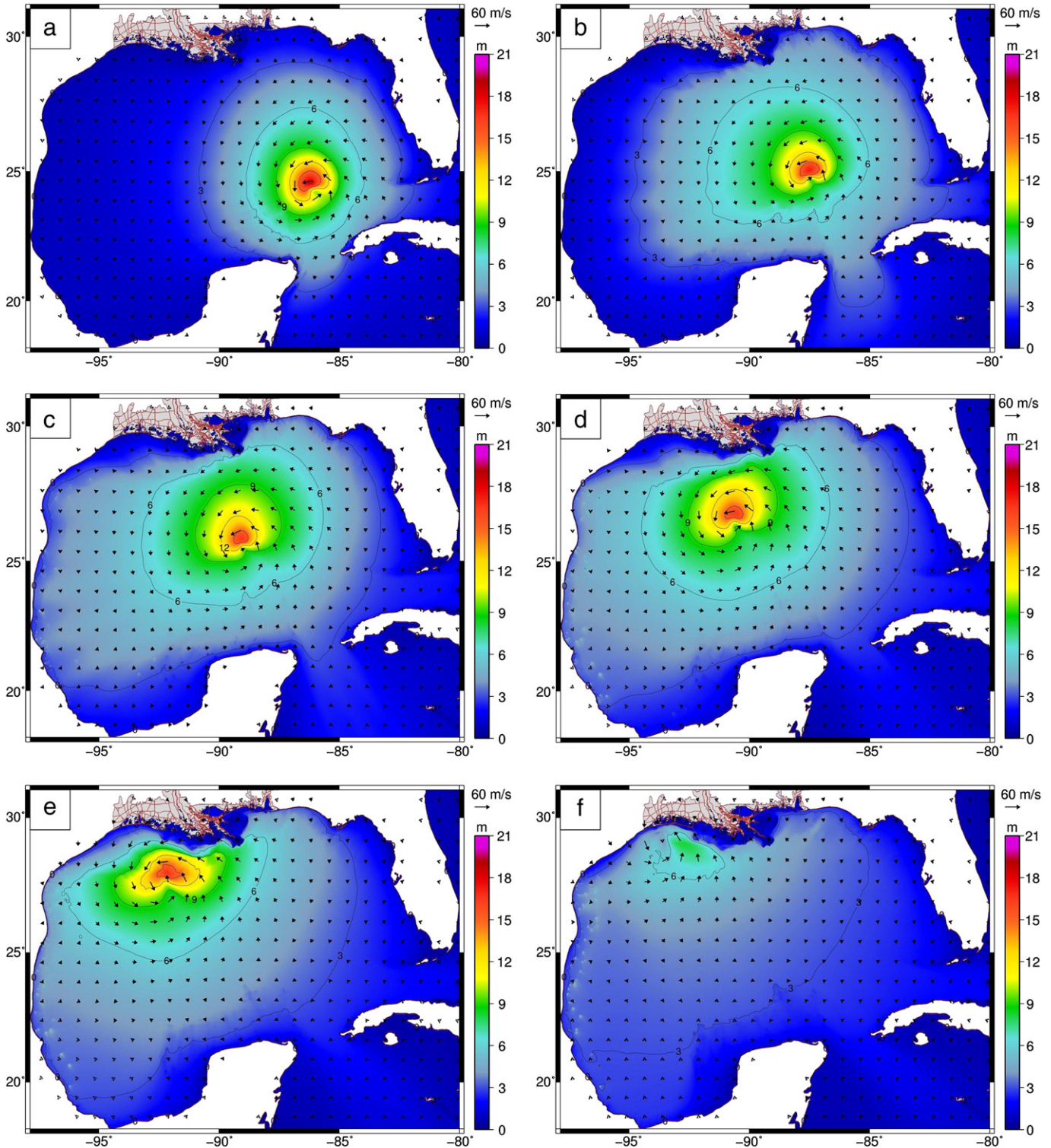

Fig. 15. Hurricane Rita significant wave height contours (m) and wind speed vectors (m s^{-1}) at 12-h intervals in the Gulf of Mexico. The six panels correspond to the following times: (a) 1800 UTC 21 September 2005, (b) 0600 UTC 22 September 2005, (c) 1800 UTC 22 September 2005, (d) 0600 UTC 23 September 2005, (e) 1800 UTC 23 September 2005 and (f) 0600 UTC 24 September 2005.

islands, whereas SWAN wave breaking is spread farther onto the continental shelf.

3.3. Hurricane Rita

Like Katrina, Rita was a powerful and destructive hurricane during the 2005 season. However, it pushed farther to the west and made landfall near the Louisiana–Texas border. In southwest Louisiana, a broad continental shelf distributed the wave breaking over a larger distance, while the lack of protruding geographic features prevented the early build-up of storm surge. These distinctions caused waves to develop and propagate differently during Rita, thus making it a good test of SWAN + ADCIRC.

3.3.1. Evolution of waves in deep water

Rita created large waves throughout the Gulf of Mexico. As shown in Fig. 15a, 60 h before landfall, the storm was well into the Gulf and was generating waves with significant heights very near their maximum of about 19 m. In addition, waves of 3–6 m propagate throughout most of the Gulf. Rita moved northwestward through the region, threatening Galveston and the Texas coastline before turning northward to make landfall at Sabine Pass. On 23 September 2005, the storm reached the continental shelf break, and its largest waves began to spread and break. The symmetry of the wave field deteriorates as the largest waves reach the shelf as shown in Fig. 15d and e. Finally, as Rita moved over the shelf and made landfall, as shown in Fig. 15f, the largest significant wave heights it generated were about 8 m. These waves broke near the coastline and created set-up and currents in southwest Louisiana.

3.3.2. Interaction of processes at landfall

We examine all aspects of the coupled system as they interact at 0600 UTC 24 September 2005, when Rita was located about 35 km and 2 h from landfall. As shown in Fig. 16a, its eye was located on the continental shelf, and its maximum wind speeds reduced to 40–45 m s^{-1}. Because of the storm's northwestward track, its winds blew parallel to the coastline in southwest Louisiana for hours before landfall. It is only at this relatively late stage in the hurricane that the winds are changing to blow inland.

The shelf has a dramatic effect on the SWAN wave solution. In Fig. 16b, the significant wave heights decreased from their maximum of about 19 m in the Gulf; now the maximum wave heights are about 8 m. Note the depth-induced breaking as the waves approach the coastline, and especially near the Tiger and Trinity Shoals (shown in Fig. 7). The wave heights decrease to 2.5–3 m over the shoals and less at the coastline. Waves of 1–1.5 m are generated inside Vermilion Bay, while waves of 1 m are generated inside Calcasieu and White Lakes. This behavior is also seen in Fig. 16c, in which sharp gradients in the mean wave periods are observed in the wave-breaking zones, and smaller periods are seen in the bays and lakes. A broad swath of mean periods of 7–9 s exists on the continental shelf, but the periods decrease as the large waves break.

As shown in Fig. 16d, the radiation stress gradients are near their maximum in regions with significant wave breaking, such as along the coastline and the shoals. The radiation stress gradients reach 0.005–0.02 m^2 s^{-2} in these regions. However, significant gradients are also located at the northeast shores of the inland water bodies and channels, as waves break in these regions. The largest gradients occur to the east, nearer to Timbalier Bay, where the hurricane is pushing
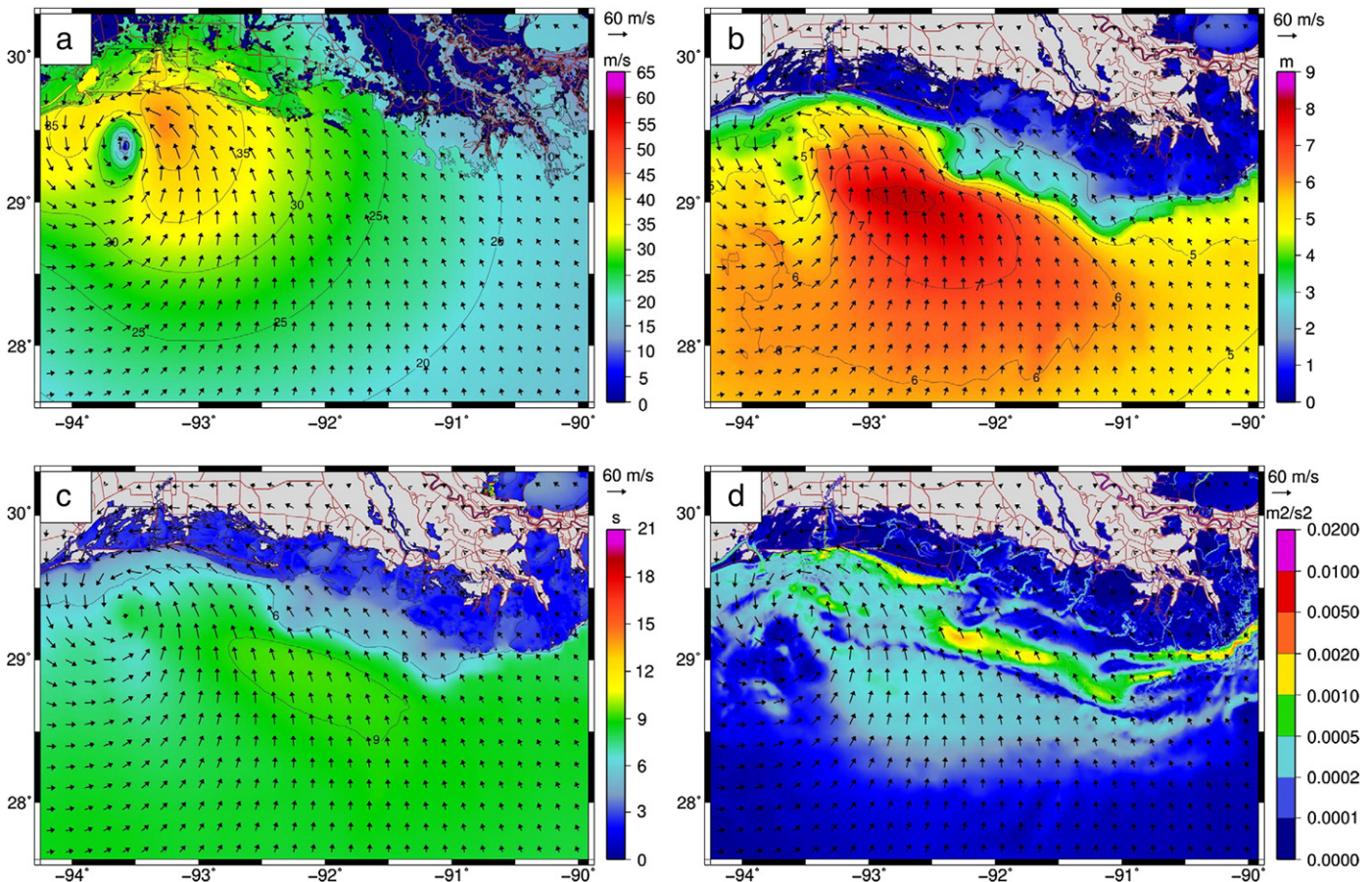

Fig. 16. Hurricane Rita winds and waves at 0600 UTC 24 September 2005 in southeastern Louisiana. The panels are: (a) wind contours and vectors (m s^{-1}), shown with a 10 min averaging period and at 10 m elevation; (b) significant wave height contours (m) and wind vectors (m s^{-1}); (c) mean wave period contours (s) and wind vectors (m s^{-1}); and (d) radiation stress gradient contours (m^2 s^{-2}) and wind vectors (m s^{-1}).

large waves onto the relatively narrow shelf, creating large radiation stress gradients and set-up.

As shown in Fig. 17a, the storm surge has not yet pushed coastal water onshore, but the overland flooding due to the lakes and bays is evident. In the four lakes, strong east–west gradients are observed, with eastern drawdown and western flooding. Easterly winds have pushed water from these lakes and into the surrounding marshes. Storm surge builds at the coastline as the winds change to blow onshore; the maximum storm surge of 4.7 m occurs near Calcasieu Pass as Rita makes landfall. As shown in Fig. 17b, at the coastline near Sabine and Calcasieu Lakes, the wave set-up is about 0.05–0.1 m, while it is 0.1–0.2 m near Vermilion Bay. The difference is caused by the shoals, which reach farther onto the shelf, where the larger waves are breaking. This set-up represents 2–5% of the overall water levels near the coastline, and 10–20% of the overall water levels farther inland.

The winds and waves also drive currents, as shown in Fig. 17c. In the region nearest the eye of the hurricane and its maximum-strength winds, the currents range from 1 to 2 m s^{-1}. The winds have developed surge on the continental shelf, and now they are pushing it into southwest Louisiana. There are also several localized instances of significant currents, such as the channel connecting Vermilion Bay to the Gulf, where the currents range from 1.5 to 2 m s^{-1} as water flows into the bay. Currents are caused by gradients in the water levels, but they are also caused by the wave breaking, as shown in Fig. 17d. The wave-driven currents are focused where the waves break, including in the channel near Vermilion Bay, along the coastline and near the shoals.

3.3.3. Validation of coupled model

The SWAN wave solution for Rita has been compared to measured results from NDBC buoys. The significant wave heights in Fig. 18 match well in regions with sufficient resolution, including the buoys on the continental shelf on either side of the storm track. At some stations near the track, however, the match is not as good. At buoy 42001, over which Rita passed while it was still a category-4 storm, the modeled peak height of 15 m is much larger than the measured peak height of 11 m. The mesh resolution of 12–18 km may be too large in this region. The mean directions (Fig. 19) and mean periods (Fig. 20) also show good agreement. At buoys to the east of the track, the waves change directions from northerly (0°) to southerly (180°) as the storm passes. This trend is reversed to the west of the track, as the waves change directions from easterly (90°) to northerly (0°). As the storm passes these buoys, the periods roughly double, from 4–6 s to about 10–12 s, and then decrease slowly as long waves continue to be generated by the storm. As shown in Table 3, the SWAN and WAM results are comparable, with average SI errors for the significant wave heights of 0.35 and 0.32, respectively. On a mesh with much coarser resolution in deep water, SWAN is similar to WAM, while offering increased resolution near the coastline and the efficiencies associated with tight coupling.

In shallow water, SWAN has been validated to the CSI measured data shown in Fig. 21. Note the gauge at station CSI06 failed during Katrina and had not been repaired when Rita passed through the Gulf. However, modeled SWAN results match well with the measured data at CSI05. The significant wave heights reach their maximum of about 2.5 m as the storm moved toward landfall, and
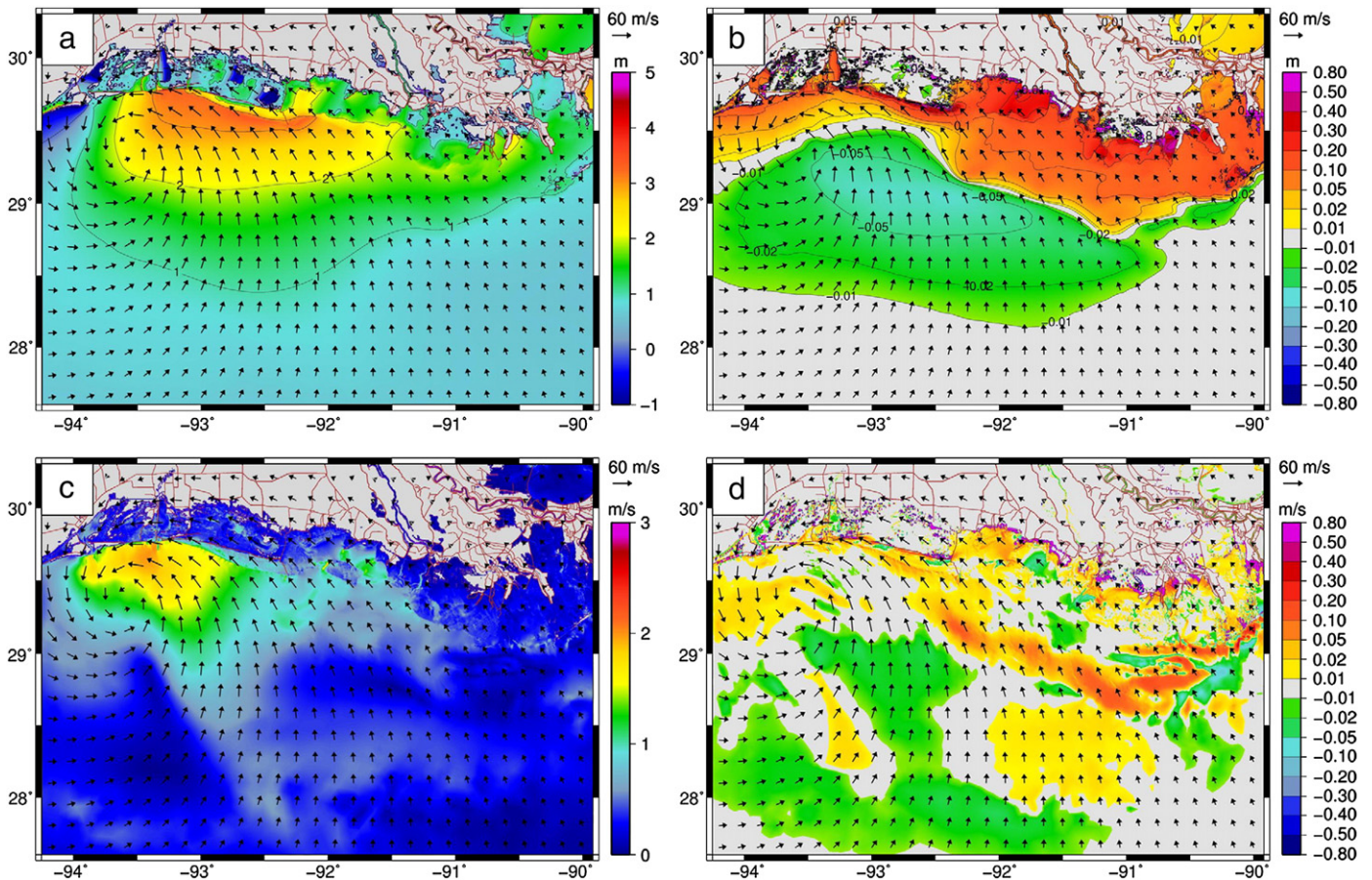

Fig. 17. Hurricane Rita water levels and currents at 0600 UTC 24 September 2005 in southeastern Louisiana. The panels are: (a) water level contours (m) and wind vectors (m s^{-1}); (b) wave-driven set-up contours (m) and wind vectors (m s^{-1}); (c) current contours (m s^{-1}) and wind vectors (m s^{-1}); and (d) wave-driven current contours (m s^{-1}) and wind vectors (m s^{-1}).
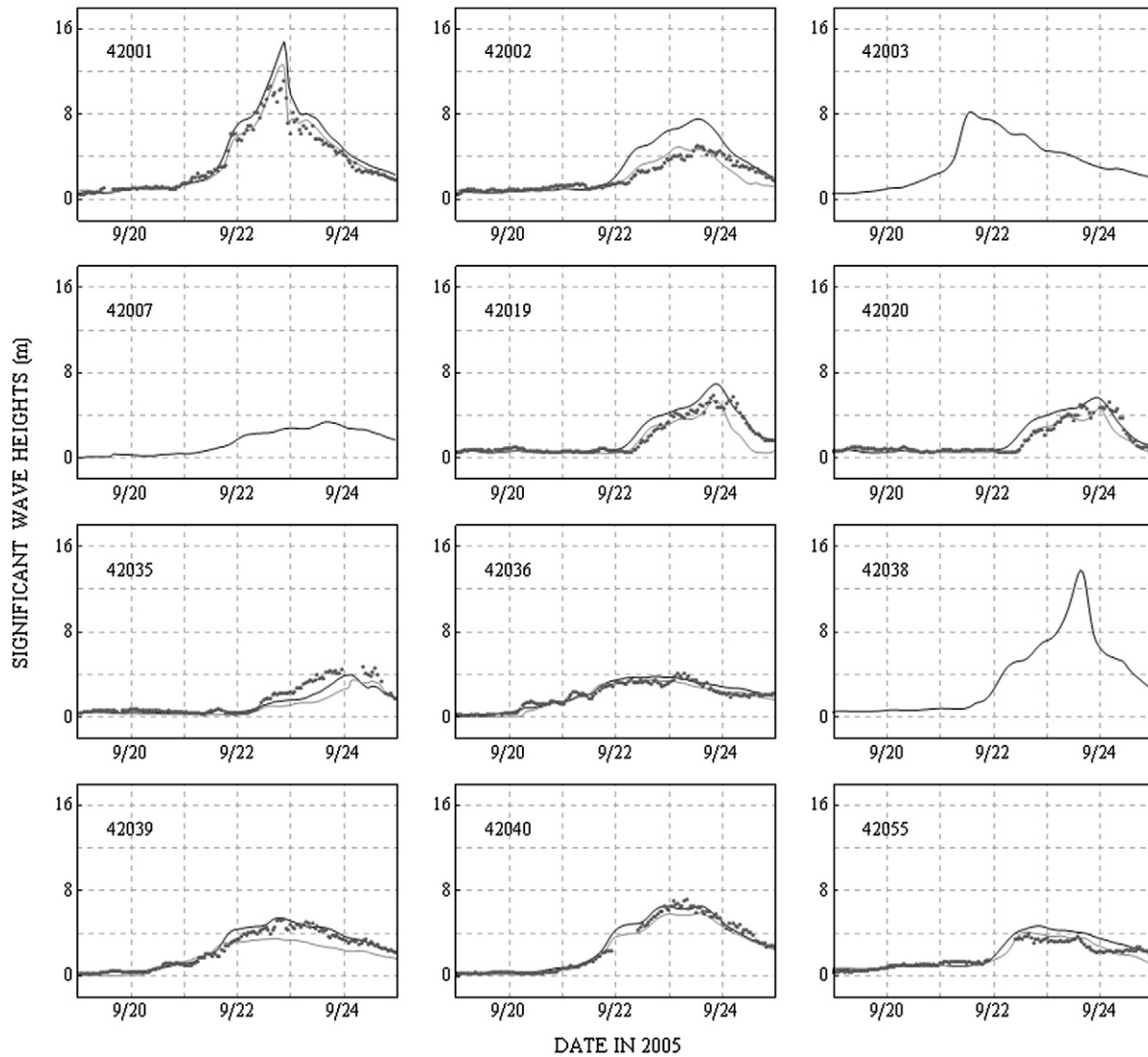
Fig. 18. Significant wave heights (m) during Hurricane Rita at 12 NDBC buoys. The measured data is shown with black dots, the modeled SWAN results are shown with black lines, and the modeled WAM results are shown with gray lines.

the mean periods jumped from about 5 s to 7–8 s. As shown in Table 4, the average errors produced by WAM/STWAVE are somewhat smaller than to those produced by SWAN, presumably because of the better estimate of the deep-water wave conditions (see previous discussion). A better representation of wave physics in the deeper Gulf in SWAN might lead to better results at these nearshore stations.

The ADCIRC solution has been validated to a set of 80 high-water marks collected by URS/FEMA (URS, 2006b). ADCIRC matches well the HWMs, with most points falling within an error of 0.5 m. A comparison of measured-to-modeled HWMs shows a best-fit slope of 0.94 and a correlation coefficient R^2 of 0.75. The significant differences occur near Vermilion Bay, where the modeled HWMs are much lower than those measured by URS/FEMA. This could be due to a lack of mesh resolution in this region or the viscous muddy bottom of Vermilion Bay (Sheremet et al., 2005; Stone et al., 2003). The removal of these points from the error statistics would increase the best-fit slope to 1.01 and the correlation coefficient R^2 to 0.85. As noted in Table 5, when the HWM uncertainties are disregarded, the estimated average absolute model error is 0.18–0.24 m, and the standard deviation is 0.33–0.39 m. These results are similar to the loose coupling of ADCIRC with WAM and STWAVE (Bunya et al., 2010).

3.4. Computational performance

SWAN + ADCIRC was benchmarked on Ranger, which is a Sun Constellation Linux Cluster at the Texas Advanced Computing Center (TACC) (http://www.tacc.utexas.edu). Ranger consists of 3936 SMP compute nodes, each with four quad-core AMD Opteron processors. The nodes are connected with an InfiniBand network with a bandwidth of 1 GB s^{-1}. The overall system has 62,976 cores, 123 TB of memory and a theoretical peak performance of 579 TFLOPS.

The Katrina simulation described previously was run with the coupled model and again with its individual components in order to discern coupling effects on simulation times. When ADCIRC was run individually, it did not receive radiation stress gradients from any source. When SWAN was run individually, it read the wind speeds from external files, but it did not receive water levels or currents from any source. The models were run on 256 to 5120 cores, of which ten cores were always dedicated for file output by ADCIRC. Wall-clock times were reported by the Sun Grid Engine batch system.

As shown in Fig. 22, the individual SWAN and ADCIRC models both scale linearly through about 1000–1500 cores, but they diverge at higher numbers of computational cores. ADCIRC's timing results level off, because the global communication associated with its implicit, conjugate-gradient solver begins to dominate the simulation time.
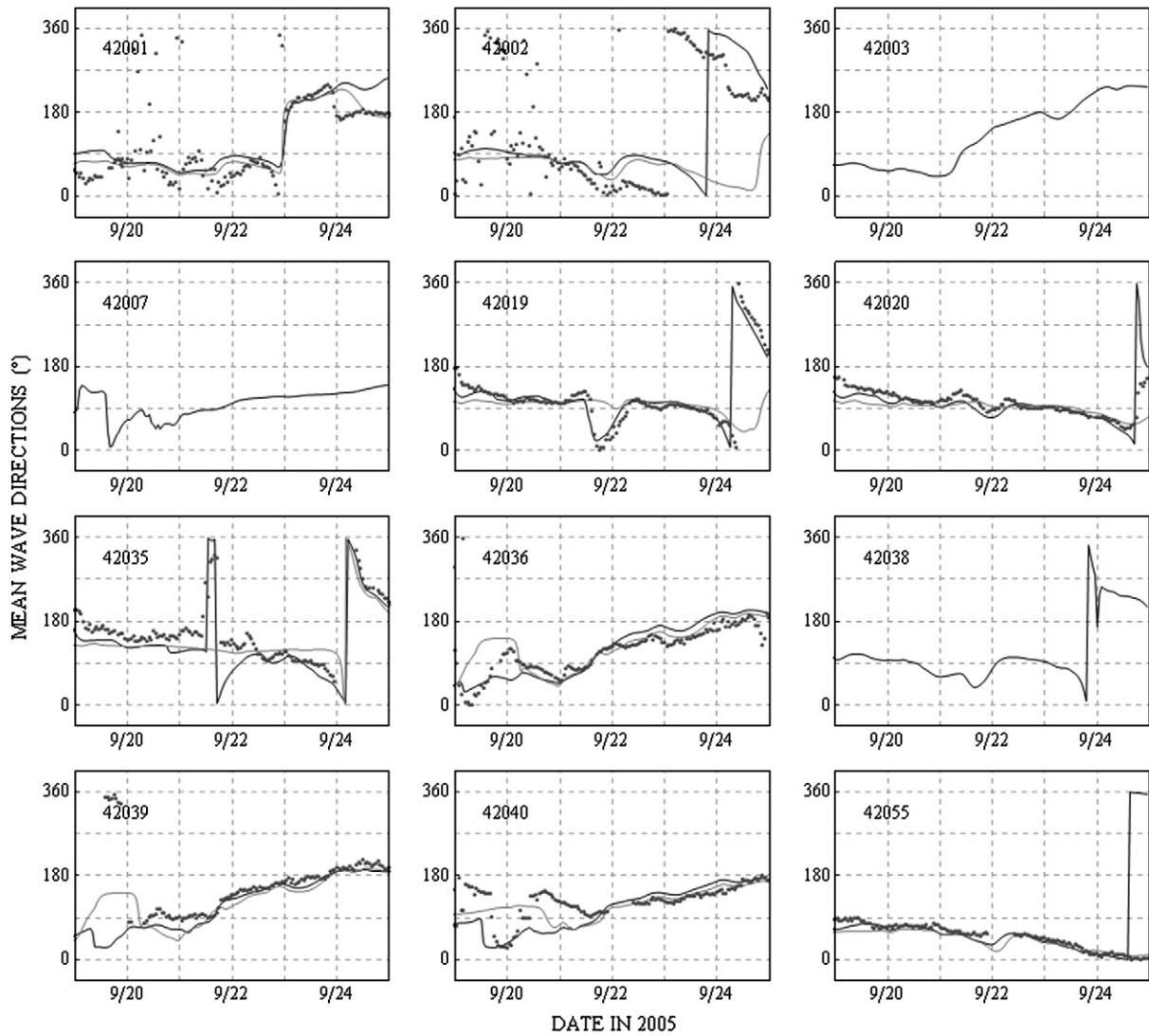
Fig. 19. Mean wave directions (°), measured clockwise from geographic north, during Hurricane Rita at 12 NDBC buoys. The measured data is shown with black dots, the modeled SWAN results are shown with black lines, and the modeled WAM results are shown with gray lines.

The highly localized solution procedure in SWAN allows it to scale linearly through 5000 cores, enabling performance of less than 10 min per day of Katrina simulation.

In the SWAN + ADCIRC timing results, note the sharp increase in performance between 246 and 374 computational cores, which suggests that the coupled model requires less than about 8000 mesh vertices per core to maintain memory in cache. Also note that the coupled model shows linear scaling to about 3000 computational cores, but then it levels off. At this point, the communication overhead from ADCIRC slows down the coupled model. However, the performance in this range is about 24 min per day of Katrina simulation, which is sufficient for forecasts of large storms.

With the exception of the run on 246 cores, when the combined problem size was too large to maintain in cache, the SWAN + ADCIRC timing results are never larger than the combination of the timing results from each component. The tight coupling adds no overhead to the simulation, and it even increases the efficiency at large numbers of cores. For example, at 3062 cores, the SWAN + ADCIRC timing of 24 min per day is less than the combined total of 20 min per day for ADCIRC and 11 min per day for SWAN. This efficiency is created by the sharing of tasks, such as the reading and interpolation of the wind input files. In addition, the computational load per file output interval is increased in the coupled model, so the dedicated file output cores

have more time to complete their tasks while the computational cores are working. Thus, at large numbers of cores, it is faster to run the coupled model than its components individually.

4. Conclusions

The recent introduction of the unstructured-mesh SWAN allows for wave simulation on the same unstructured meshes used by ADCIRC, which utilizes basin-to-floodplain scale domains and increases locally the resolution in regions with large spatial gradients. This work implemented the tight coupling of SWAN + ADCIRC, so that these models run as an integrated system on the same mesh, and vertex-based solutions and forcing information are passed through local memory or cache.

SWAN + ADCIRC simulates hurricane storm surge with high levels of accuracy. Hindcasts of Katrina and Rita show that the models generate waves in deep water; dissipate waves due to changes in wave–wave interactions, bathymetry and bottom friction in southern Louisiana; apply the radiation stress gradients to create set-up and wave-driven currents in the circulation model; and then return those water levels and currents to the wave model. SWAN compares well to measured wave parameters at 12 NDBC buoys in the Gulf, even though the mesh resolution is 12–18 km in those areas. Major
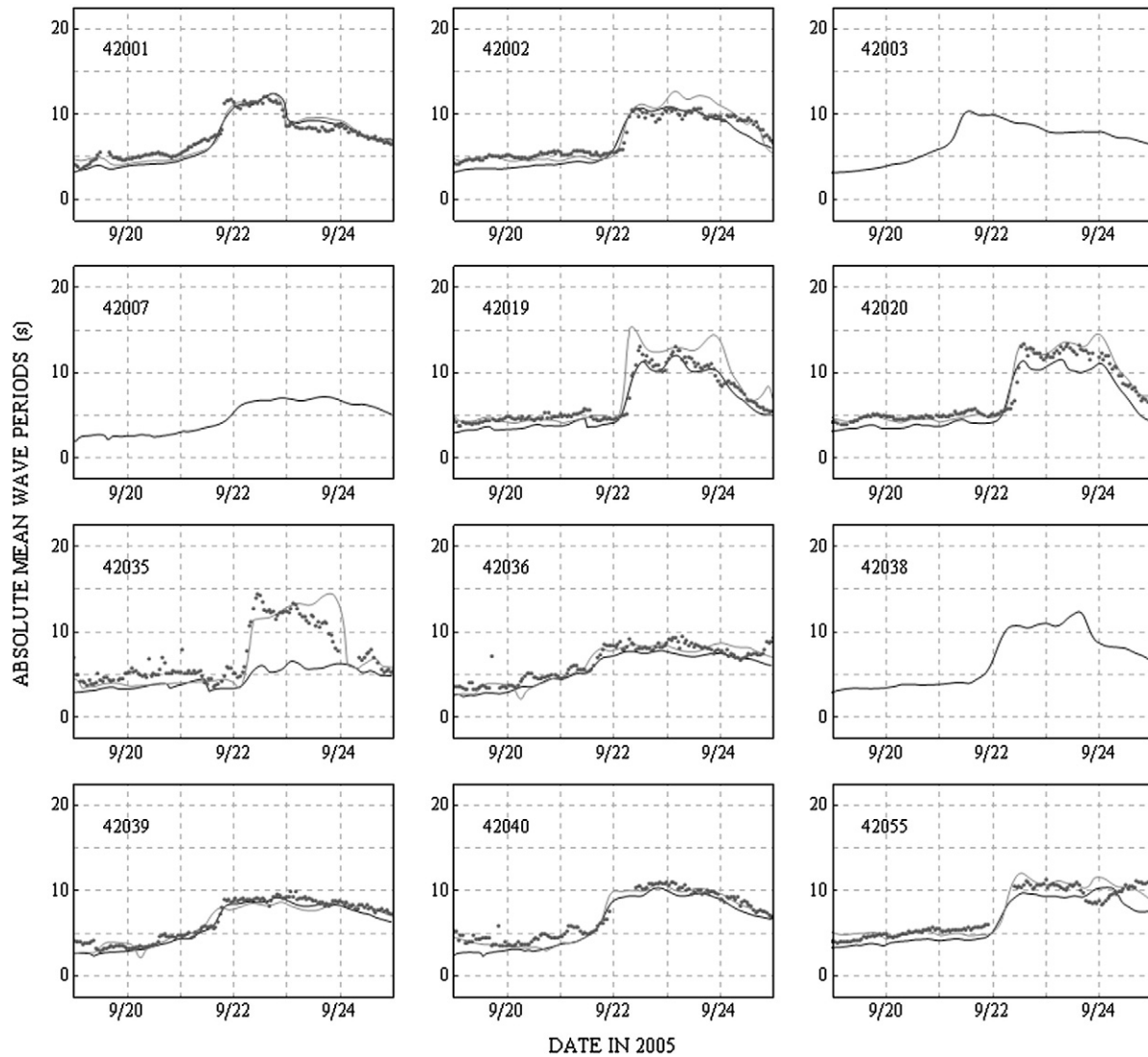
Fig. 20. Mean wave periods (s) during Hurricane Rita at 12 NDBC buoys. The measured data is shown with black dots, the modeled SWAN results are shown with black lines, and the modeled WAM results are shown with gray lines.

differences were at buoys located west of the hurricane track, where SWAN + ADCIRC tends to over-predict the significant wave heights. This over-prediction may be due to missing physics (such as the warm-core eddy) or poor numerics (such as the coarseness of the mesh). In the nearshore, validation of SWAN to measured data at two CSI stations showed that SWAN matches well the wave behavior on the continental shelf. The ADCIRC modeled water levels compare well with measured HWMs. Comparisons to WAM and STWAVE showed that the errors in the SWAN results are slightly larger than in the WAM/STWAVE results, which may be due to a larger mesh size for SWAN in deep water. SWAN's physics can be optimized for deep

water, and it is well-positioned to increase its localized resolution to improve accuracy in the future.

SWAN + ADCIRC is also highly efficient. It eliminates the need for interpolation between models with heterogeneous meshes, interpolation at the boundaries of nested meshes, and the consideration of overlapping or inconsistent solutions. It shows linear scaling to about 2000 cores and wall-clock times of 24 min per day of Katrina simulation on a mesh with 2.4 million vertices. The coupled model maintains linear scaling to larger numbers of computational cores when applied to meshes with larger numbers of vertices. It does not add overhead due to interpolation, global communication or the

Table 3
Summary of average errors at the NDBC buoys for the SWAN and WAM simulations of Katrina and Rita during the time periods shown in Table 2. The Scatter Index (SI) and Relative Bias error metrics were computed using Eqs. (12) and (13) (but they have not been normalized for the mean directions). The differences in the mean observations for each model reflect the differences in the time periods over which the errors were computed.

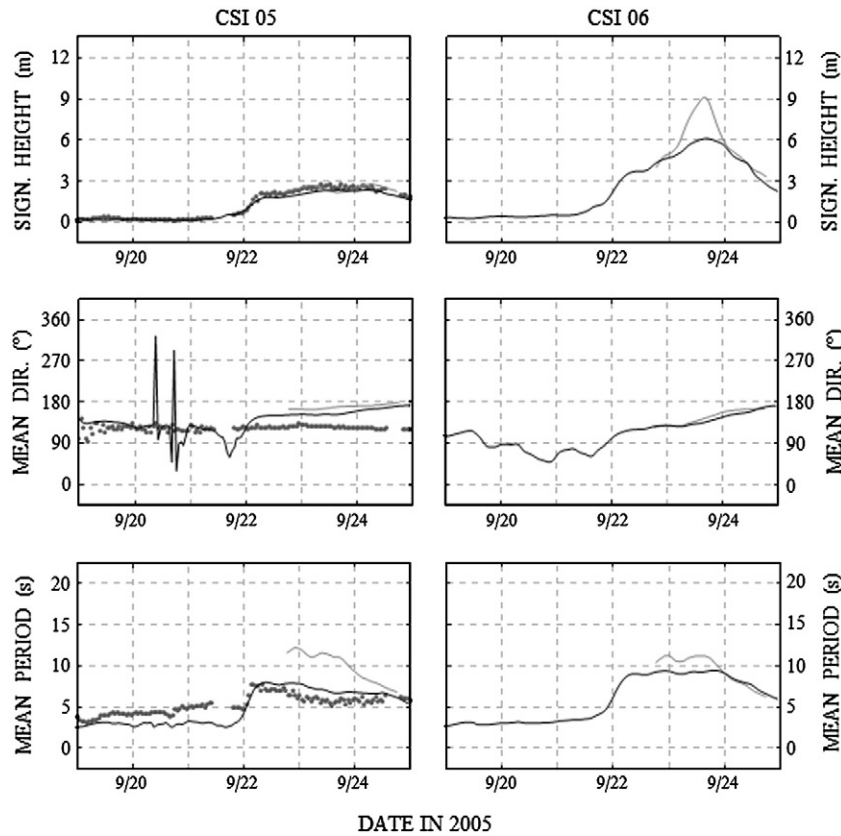| Storm	Model	Significant heights			Mean directions			Mean periods		
		SI	Relative Bias	Mean Obs. (m)	RMS (°)	Bias (°)	Mean Obs. (°)	SI	Relative Bias	Mean Obs. (s)
Katrina	SWAN	0.44	0.077	1.87	37.8	−9.0	136.7	0.22	−0.140	6.53
	WAM	0.36	−0.038	1.71	49.7	−13.0	134.7	0.18	0.182	6.43
Rita	SWAN	0.35	0.094	1.98	36.5	0.9	126.5	0.21	−0.156	6.74
	WAM	0.32	−0.104	1.97	45.1	0.2	127.0	0.16	0.012	6.73

Fig. 21. Hurricane Rita significant wave heights (m); mean wave directions (°), measured clockwise from geographic north; and mean wave periods (s) at two CSI buoys. The measured data is shown with black dots, the modeled SWAN results are shown with black lines, and the modeled STWAVE results are shown with gray lines. Note that buoy CSI 06 did not record during the storm. The CSI buoy data was collected by WAVCIS (http://www.wavcis.lsu.edu).

Table 4
Summary of errors for the SWAN and WAM/STWAVE simulations of Katrina and Rita during the time periods shown in Table 2. Note that buoy CSI06 did not record during Rita. The Scatter Index (SI) and Relative Bias error metrics were computed using Eqs. (12) and (13) (but they have not been normalized for mean directions). The differences in the mean observations for each model reflect the differences in the time periods over which the errors were computed.

Storm	Gauge	Model	Significant heights			Mean directions			Mean periods		
			SI	Relative Bias	Mean Obs. (m)	RMS (°)	Bias (°)	Mean Obs. (°)	SI	Relative Bias	Mean Obs. (s)
Katrina	CSI05	SWAN	0.34	−0.029	0.73	52.7	21.0	123.9	0.29	−0.174	4.84
		WAM/STWAVE	0.20	0.073	1.70	75.6	61.5	120.8	0.70	0.510	5.67
	CSI06	SWAN	0.16	−0.001	0.90	64.1	−34.4	132.9	0.32	−0.249	5.14
		WAM/STWAVE	0.06	0.030	3.87	25.2	−23.3	143.8	0.29	0.291	8.25
Rita	CSI05	SWAN	0.18	−0.127	1.13	40.2	22.8	123.5	0.25	−0.084	5.03
		WAM/STWAVE	0.10	−0.002	2.50	44.4	43.9	124.5	0.78	0.741	5.90
	CSI06	SWAN	–	–		–	–		–	–	
		WAM/STWAVE	–	–		–	–		–	–	

mechanics of managing the coupling. Instead, SWAN + ADCIRC shares the work among model components in a way that can speed up the combined run time. The result is a coupled model that is well-positioned for applications in high-performance computing environments.

Future work will improve the efficiency and accuracy of the coupled model. The new generation of computational meshes in southern Louisiana and Texas will increase resolution in the wave-generation zones in the Gulf of Mexico, the wave-breaking zones along the coastline and the barrier islands, and the channels and inlets

Table 5
Summary of difference/error statistics for the Katrina and Rita HWM data sets. Average absolute differences/errors and standard deviations are given in m.

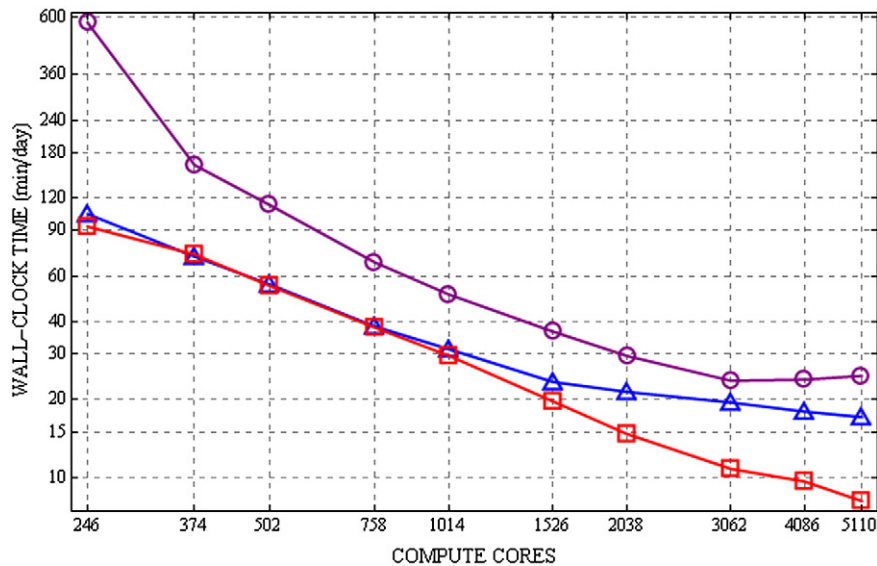| Storm	Data set	ADCIRC to measured HWMs		Measured HWMs		Estimated ADCIRC errors	
		Average absolute difference	Standard deviation	Average absolute difference	Standard deviation	Average absolute error	Standard deviation
Katrina	USACE	0.40	0.47	0.13	0.18	0.27	0.44
Katrina	URS	0.36	0.44	0.10	0.16	0.26	0.41
Rita	URS	0.34	0.43	0.10	0.18	0.24	0.39
Rita (no VB)	URS	0.28	0.38	0.11	0.19	0.18	0.33

Fig. 22. Timing results for SWAN + ADCIRC and its components on the TACC Ranger machine. The times shown are wall-clock minutes per day of Katrina simulation on the SL15 mesh. SWAN results are shown in red, ADCIRC results are shown in blue, and SWAN + ADCIRC results are shown in purple.

further inland. Future generations of meshes will relax initially the resolution and then refine adaptively, by adding resolution in regions where the computed gradients are large in either model component. These meshes will represent better the wave and circulation solutions, and the highly-efficient, coupled model will allow them to be used operationally. The tight coupling of SWAN + ADCIRC enables waves, water levels and currents to interact in complex problems and in a way that is accurate and efficient.

Acknowledgements

References

Atkinson, J.H., Westerink, J.J., Hervouet, J.M., 2004. Similarities between the wave equation and the quasi-bubble solutions to the shallow water equations. International Journal for Numerical Methods in Fluids 45, 689–714.

Battjes, J.A., 1972. Radiation stresses in short-crested waves. Journal of Marine Research 30 (1), 56–64.

Battjes, J.A., Janssen, J.P.F.M., 1978. Energy loss and set-up due to breaking of random waves. Proceedings of the 16th International Conference on Coastal Engineering, ASCE, pp. 569–587.

Booij, N., Ris, R.C., Holthuijsen, L.H., 1999. A third-generation wave model for coastal regions, Part I, model description and validation. Journal of Geophysical Research 104, 7649–7666.

Bunya, S., Dietrich, J.C., Westerink, J.J., Ebersole, B.A., Smith, J.M., Atkinson, J.H., et al., 2010. A high resolution coupled riverine flow, tide, wind, wind wave and storm surge model for southern Louisiana and Mississippi: Part I — model development and validation. Monthly Weather Review 138, 345–377.

Cardone, V.J., Jensen, R.E., Resio, D.T., Swail, V.R., Cox, A.T., 1996. Evaluation of contemporary ocean wave models in rare extreme events: the "Halloween Storm" of October 1991 and the "Storm of the Century" of March 1993. Journal of Atmospheric and Oceanic Technology 13 (1), 198–230.

Cardone, V.J., Cox, A.T., Forristall, G.Z., 2007. OTC 18652: hindcast of winds, waves and currents in Northern Gulf of Mexico in Hurricanes Katrina (2005) and Rita (2005). 2007 Offshore Technology Conference, Houston, TX.

Chen, Q., Wang, L., Tawes, R., 2008. Hydrodynamic response of Northeastern Gulf of Mexico to hurricanes. Estuaries and Coasts 31 (6), 1098–1116.

Collins, N., Theurich, G., DeLuca, C., Suarez, M., Trayanov, A., Balaji, V., et al., 2005. Design and implementation of components in the earth system modeling framework. International Journal of High Performance Computing Applications 19 (3), 341–350.

Cox, A.T., Greenwood, J.A., Cardone, V.J., Swail, V.R., 1995. An interactive objective kinematic analysis system. Fourth International Workshop on Wave Hindcasting and Forecasting, Banff, Alberta. Atmospheric Environment Service, Canada, pp. 109–118.

Dawson, C., Westerink, J.J., Feyen, J.C., Pothina, D., 2006. Continuous, discontinuous and coupled discontinuous–continuous galerkin finite element methods for the shallow water equations. International Journal for Numerical Methods in Fluids 52, 63–88.

Dietrich, J.C., Bunya, S., Westerink, J.J., Ebersole, B.A., Smith, J.M., Atkinson, J.H., et al., 2010. A high resolution coupled riverine flow, tide, wind, wind wave and storm surge model for southern Louisiana and Mississippi: Part II — synoptic description and analyses of Hurricanes Katrina and Rita. Monthly Weather Review 138, 378–404.

Ebersole, B.A., Westerink, J.J., Resio, D.T., Dean, R.G., 2007. Performance evaluation of the New Orleans and Southeast Louisiana Hurricane Protection System, Volume IV — the storm. Final Report of the Interagency Performance Evaluation Task Force. U.S. Army Corps of Engineers, Washington, D.C.

Eldeberky Y. Nonlinear transformation of wave spectra in the nearshore zone. Ph.D. thesis, Delft University of Technology, Delft, The Netherlands 1996.

Funakoshi, Y., Hagen, S.C., Bacopoulos, P., 2008. Coupling of hydrodynamic and wave models: case study for Hurricane Floyd (1999) hindcast. ASCE Journal of Waterway, Port, Coastal and Ocean Engineering 134 (6), 321–335.

Garratt, J.R., 1977. Review of drag coefficients over oceans and continents. Monthly Weather Review 105, 915–929.

Gorman, R.M., Neilson, C.G., 1999. Modelling shallow water wave generation and transformation in an intertidal estuary. Coastal Engineering 36, 197–217.

Gregersen, J.B., Gijsbers, P.J.A., Westen, S.J.P., Blind, M., 2005. OpenMI: the essential concepts and their implications for legacy software. Advances in Geosciences 4, 37–44.

Gunther, H., 2005. WAM Cycle 4.5 Version 2.0, Institute for Coastal Research. GKSS Research Centre Geesthacht.

Hasselmann, K., 1974. On the spectral dissipation of ocean waves due to whitecapping. Boundary-Layer Meteorology 6, 107–127.

Hasselmann, K., Barnett, T.P., Bouws, E., Carlson, H., Cartwright, D.E., Enke, K., et al., 1973. Measurements of wind–wave growth and swell decay during the Joint North Sea Wave Project (JONSWAP). Ergnzungsheft zur Deutschen Hydrographischen Zeitschrift Reihe 12 (A8).

Hasselmann, S., Hasselmann, K., Allender, J.H., Barnett, T.P., 1985. Computations and parameterizations of the nonlinear energy transfer in a gravity wave spectrum. Part II: parameterizations of the nonlinear transfer for application in wave models. Journal of Physical Oceanography 15 (11), 1378–1391.

Hill, C., DeLuca, C., Balaji, V., Suarez, M., da Silva, A., 2004. Architecture of the Earth System Modeling Framework. Computing in Science and Engineering 6 (1).

Holthuijsen, L.H., Herman, A., Booij, N., 2003. Phase-decoupled refraction–diffraction for spectral wave models. Coastal Engineering 49, 291–305.

Janssen, P., 2004. The Interaction of Ocean Waves and Wind. Cambridge University Press, Cambridge.

Karypis, G., Kumar, V., 1999. A fast and high quality multilevel scheme for partitioning irregular graphs. SIAM Journal of Scientific Computing 20 (1), 359–392.

Kim, S.Y., Yasuda, T., Mase, H., 2008. Numerical analysis of effects of tidal variations on storm surges and waves. Applied Ocean Research 30, 311–322.

Kolar, R.L., Westerink, J.J., Cantekin, M.E., Blain, C.A., 1994. Aspects of nonlinear simulations using shallow water models based on the wave continuity equations. Computers and Fluids 23 (3), 1–24.

Komen, G., Cavaleri, L., Donelan, M., Hasselmann, K., Hasselmann, S., Janssen, P.A.E.M., 1994. Dynamics and Modeling of Ocean Waves. Cambridge University Press, Cambridge.

Longuet-Higgins, M.S., Stewart, R.W., 1964. Radiation stresses in water waves; physical discussions, with applications. Deep Sea Research 11, 529–562.

Luettich, R.A., Westerink, J.J., 2004. Formulation and numerical implementation of the 2D/3D ADCIRC Finite Element Model Version 44.XX. http://adcirc.org/adcirc_theory_2004_12_08.pdf2004.

Moore, R.V., Tindall, I., 2005. An overview of the open modelling interface and environment (the OpenMI). Environmental Science and Policy 8, 279–286.

Pandoe, W.W., Edge, B.L., 2008. Case study for a cohesive sediment transport model for Matagorda Bay, Texas, with coupled ADCIRC 2D-Transport and SWAN Wave Models. ASCE Journal of Hydraulic Engineering 134 (3), 303–314.

Powell, M., Houston, S., Reinhold, T., 1996. Hurricane Andrew's landfall in South Florida. Part I: standardizing measurements for documentation of surface windfields. Weather Forecasting 11, 304–328.

Powell, M., Houston, S., Amat, L., Morrisseau-Leroy, N., 1998. The HRD real-time hurricane wind analysis system. Journal of Wind Engineering and Industrial Aerodynamics 77–78, 53–64.

Ris, R.C., Booij, N., Holthuijsen, L.H., 1999. A third-generation wave model for coastal regions, Part II, verification. Journal of Geophysical Research 104, 7667–7681.

Rogers, W.E., Hwang, P.A., Wang, D.W., 2003. Investigation of wave growth and decay in the SWAN model: three regional-scale applications. Journal of Physical Oceanography 33, 366–389.

Sheremet, A., Mehta, A.J., Liu, B., Stone, G.W., 2005. Wave–sediment interaction on a muddy inner shelf during Hurricane Claudette. Estuarine, Coastal and Shelf Science 63, 225–233.

Smith, J.M., Sherlock, A.R., Resio, D.T., 2001. *STWAVE: Steady-State Spectral Wave Model User's Manual for STWAVE, Version 3.0*. USACE, Engineer Research and Development Center. Technical Report ERDC/CHL SR-01-1, Vicksburg, MS. http://chl.erdc.usace.army.mil/Media/2/4/4/erdc-chl-sr-01-11.pdf.

Snyder, R.L., Dobson, F.W., Elliott, J.A., Long, R.B., 1981. Array measurements of atmospheric pressure fluctuations above surface gravity waves. Journal of Fluid Mechanics 102, 1–59.

Stone, G.W., Sheremet, A., Zhang, X., He, Q., Liu, B., Strong, B., 2003. Landfall of two tropical systems seven days apart along southcentral Louisiana, USA. *Proceedings of Coastal Sediments '03*, Clearwater Beach, Florida, USA, pp. 333–334.

Thompson, E.F., Smith, J.M., Miller, H.C., 2004. Wave transformation modeling at Cape Fear River Entrance, North Carolina. J. Coastal Research 20 (4), 1135–1154.

Tolman, H.L., 2009. User manual and system documentation of WAVEWATCH III version 3.14. NOAA / NWS / NCEP / MMAB Technical Note 276.

URS, 2006a. Final coastal and riverine high-water marks collection for Hurricane Katrina in Louisiana. Final Report for the Federal Emergency Management Agency.

URS, 2006b. Final coastal and riverine high-water marks collection for Hurricane Rita in Texas. Final Report for the Federal Emergency Management Agency.

WAMDI Group, 1988. The WAM model — a third generation ocean wave prediction model. J. Phys. Oceanogr. 18, 1775–1810.

Wang, D.P., Oey, L.Y., 2008. Hindcast of waves and currents in Hurricane Katrina. Bulletin of the American Meteorological Society 89 (4), 487–495.

Warner, J.C., Perlin, N., Skyllingstad, E.D., 2008. Using the model coupling toolkit to couple earth system models. Environmental Modelling & Software 23, 1240–1249.

Weaver, R.J., Slinn, D.N., 2004. Effect of wave forcing on storm surge. *Proceedings of Coastal Engineering '04*, Lisbon, Portugal, pp. 1532–1538.

Westerink, J.J., Luettich, R.A., Feyen, J.C., Atkinson, J.H., Dawson, C., Roberts, H.J., et al., 2008. A basin to channel scale unstructured grid hurricane storm surge model applied to southern Louisiana. Monthly Weather Review 136 (3), 833–864.

Wu, J., 1982. Wind-stress coefficients over sea surface from breeze to hurricane. Journal of Geophysical Research 87, 9704–9706.

Zijlema, M., 2010. Computation of wind–wave spectra in coastal waters with SWAN on unstructured grids. Coastal Engineering 57, 267–277.